51030

0-315-03134-4

National Library of Canada / Bibliothèque nationale du Canada

CANADIAN THESES ON MICROFICHE / THÈSES CANADIENNES SUR MICROFICHE

NAME OF AUTHOR/*NOM DE L'AUTEUR* David R. Karecki

TITLE OF THESIS/*TITRE DE LA THÈSE* Far-infrared study of the charge-density-wave states of 1T-TaS_2 and 1T-$TaSe_2$

UNIVERSITY/*UNIVERSITÉ* Simon Fraser University

DEGREE FOR WHICH THESIS WAS PRESENTED/ *GRADE POUR LEQUEL CETTE THÈSE FUT PRÉSENTÉE* Ph.D.

YEAR THIS DEGREE CONFERRED/*ANNÉE D'OBTENTION DE CE DEGRÉ* 1980

NAME OF SUPERVISOR/*NOM DU DIRECTEUR DE THÈSE* Dr. B. P. Clayman

Permission is hereby granted to the NATIONAL LIBRARY OF CANADA to microfilm this thesis and to lend or sell copies of the film.

The author reserves other publication rights, and neither the thesis nor extensive extracts from it may be printed or otherwise reproduced without the author's written permission.

L'autorisation est, par la présente, accordée à la BIBLIOTHÈQUE NATIONALE DU CANADA de microfilmer cette thèse et de prêter ou de vendre des exemplaires du film.

L'auteur se réserve les autres droits de publication; ni la thèse ni de longs extraits de celle-ci ne doivent être imprimés ou autrement reproduits sans l'autorisation écrite de l'auteur.

DATED/*DATÉ* 19 JUN 80 SIGNED/*SIGNÉ*

PERMANENT ADDRESS/*RÉSIDENCE FIXE* [redacted]

NL-91 (11-79)

National Library of Canada
Collections Development Branch

Canadian Theses on
Microfiche Service

Bibliothèque nationale du Canada
Direction du développement des collections

Service des thèses canadiennes
sur microfiche

NOTICE

The quality of this microfiche is heavily dependent upon the quality of the original thesis submitted for microfilming. Every effort has been made to ensure the highest quality of reproduction possible.

If pages are missing, contact the university which granted the degree.

Some pages may have indistinct print especially if the original pages were typed with a poor typewriter ribbon or if the university sent us a poor photocopy.

Previously copyrighted materials (journal articles, published tests, etc.) are not filmed.

Reproduction in full or in part of this film is governed by the Canadian Copyright Act, R.S.C. 1970, c. C-30. Please read the authorization forms which accompany this thesis.

THIS DISSERTATION
HAS BEEN MICROFILMED
EXACTLY AS RECEIVED

AVIS

La qualité de cette microfiche dépend grandement de la qualité de la thèse soumise au microfilmage. Nous avons tout fait pour assurer une qualité supérieure de reproduction.

S'il manque des pages, veuillez communiquer avec l'université qui a conféré le grade.

La qualité d'impression de certaines pages peut laisser à désirer, surtout si les pages originales ont été dactylographiées à l'aide d'un ruban usé ou si l'université nous a fait parvenir une photocopie de mauvaise qualité.

Les documents qui font déjà l'objet d'un droit d'auteur (articles de revue, examens publiés, etc.) ne sont pas microfilmés.

La reproduction, même partielle, de ce microfilm est soumise à la Loi canadienne sur le droit d'auteur, SRC 1970, c. C-30. Veuillez prendre connaissance des formules d'autorisation qui accompagnent cette thèse.

LA THÈSE A ÉTÉ
MICROFILMÉE TELLE QUE
NOUS L'AVONS REÇUE

Ottawa, Canada
K1A 0N4

FAR-INFRARED STUDY OF THE CHARGE-DENSITY-WAVE STATES OF 1T-TaS_2 AND 1T-$TaSe_2$

by

David Ralph Karecki

B.S., Michigan State University, 1968

M.Sc., Simon Fraser University, 1972

A THESIS SUBMITTED IN PARTIAL FULFILLMENT OF

OF THE REQUIREMENTS FOR THE DEGREE OF

DOCTOR OF PHILOSOPHY

in the Department

of

Physics

© David Ralph Karecki 1980

SIMON FRASER UNIVERSITY

May 1980

All rights reserved. This thesis may not be reproduced in whole or in part, by photocopy or other means, without permission of the author.

APPROVAL

Name: David Ralph Karecki

Degree: Doctor of Philosophy

Title of Thesis: Far-infrared Study of the Charge-Density-Wave States of 1T-TaS_2 and 1T-$TaSe_2$

Examining Committee:

Chairman: M. Plischke

B. P. Clayman
Senior Supervisor

R. F. Frindt

K. S. Viswanathan

J. C. Irwin

M. V. Klein
External Examiner
Professor
Department of Physics
University of Illinois

Date Approved: 5/22/80

PARTIAL COPYRIGHT LICENSE

I hereby grant to Simon Fraser University the right to lend my thesis or dissertation (the title of which is shown below) to users of the Simon Fraser University Library, and to make partial or single copies only for such users or in response to a request from the library of any other university, or other educational institution, on its own behalf or for one of its users. I further agree that permission for multiple copying of this thesis for scholarly purposes may be granted by me or the Dean of Graduate Studies. It is understood that copying or publication of this thesis for financial gain shall not be allowed without my written permission.

Title of Thesis/Dissertation:

Far-infrared study of the charge-density-wave states of 1T-TaS_2 and 1T-$TaSe_2$

Author:

(signature)

David R. Karecki

(name)

May 22, 1980

(date)

ABSTRACT

1T-TaS_2 and 1T-$TaSe_2$ are layered, almost two dimensional compounds with weak bonding between layers. At temperatures below 600 K, both crystals are distorted from the CdI_2 structure by an electronic instability known as a charge-density-wave (CDW). Above 180 K in 1T-TaS_2 and 473 K in 1T-$TaSe_2$, the far-infrared ($1/\lambda$ =2-500 cm^{-1}) reflectivity spectra are unremarkable and adequately explained by standard theories.

However, below these temperatures, both crystals have spectra which indicate the presence of far too many infrared-active phonons than is possible for a CdI_2 structure. At these lower temperatures, both crystals are known to have CDW distortions that are commensurate with the host CdI_2-type lattices forming a superlattice with 39 atoms in a unit cell. This large number of atoms can explain why so many phonons are observed but makes any exact model calculation intractable.

A combination of a simple lattice dynamical model and the concept of modes "folding-in" from parts of the Brillouin zone not normally accessible to optical studies can explain the origin of the observed modes. The frequencies of these modes cannot be predicted accurately due to the necessary simplicity of the model. The model does imply which modes are related to either the acoustic or optic branches of the phonon dispersion curves of the CdI_2 structure. Frequency ratios of

corresponding modes in 1T-TaS_2 and 1T-$TaSe_2$ are consistent with this interpretation.

The reflectivity spectra were fit with standard mathematical expressions. When interpreted at a microcopic level, the parameters obtained for 1T-$TaSe_2$ seem to indicate a gradual decrease in the number of free carriers or an increase in their effective mass as the temperature was lowered from 295 to 4.2 K. This is not usual metallic behavior and implies changes in the band structure as a result of interactions with the CDW.

TABLE OF CONTENTS

PAGE

Approval Page ii

Abstract iii

Table of Contents v

List of Tables vi

List of Figures vii

Chapter 1 Introduction 1

Chapter 2 Experiment 25

Chapter 3 Determination of Optical Constants 50

Chapter 4 Discussion of Phonon Results 71

Chapter 5 Discussion of Plasmons 93

Chapter 6 Summary 105

Appendix I 109

Bibliography 112

LIST OF TABLES

TABLE		PAGE
1.1	Lattice parameters of 1T-TaS_2 and 1T-$TaSe_2$ in nm	19
1.2	Optical phonon frequencies in wavenumbers for some transition metal dichalcogenides	20
2.1	Beamsplitters, filters, and their effective frequency ranges in cm^{-1}	40
3.1	Transverse optical frequencies determined from a Kramers-Kronig analysis of the 1T-TaS_2 reflectivity in the CCDW phase	61
3.2	Fitting parameters for 1T-TaS_2 at 100 K	62
3.3	Lucovsky's (1976) Lorentz parameters for 1T-$TaSe_2$ at 295 K	63
4.1	Phonon frequencies calculated by Duffey (1978) at three points in the Brillouin zone of an undistorted 1T-TaS_2 crystal	87
4.2	Dominant phonon frequencies in cm^{-1} in both 1T-TaS_2 and 1T-$TaSe_2$ in the CCDW phases along with the ratio of sulphide to selenide frequencies	88
4.3	Summary of experimental optical mode frequencies in cm^{-1} in the CCDW phase of 1T-TaS_2	89
4.4	Comparison of IR and Raman (Duffey 1978) mode frequencies in the CCDW phase of 1T-$TaSe_2$	90
4.5	Comparison of IR phonon mode frequencies in the CCDW phases of 1T-$TaSe_2$ and 1T-$TiSe_2$	91

LIST OF FIGURES

FIGURE PAGE

1.1 a) CdI_2 unit cell in basal plane
b) Commensurate unit cell showing only cations 22

1.2 Resistivity vs. temperature for 1T-TaS_2 and 1T-$TaSe_2$ taken from Wilson et al. (1975) 23

1.3 Normal modes of the 1T and 2H structures 24

2.1 Resistivity of 1T-TaS_2 vs. temperature normalized to $9X10^{-4}$ ohm-cm 41

2.2 Resistivity of 1T-$TaSe_2$ vs. temperature 42

2.3 Sample insert for reflectivity measurements at 15° incidence at liquid He temperatures 43

2.4 a) Sample configuration at 15° incidence and $T \geq 80$ K
b) Sample configuration for polarization measurements at 45 ° incidence 44

2.5 Cross-sectional view of dual-cavity 45

2.6 Reflectivity of 1T-TaS_2 at 15° incidence in the QCDW (295 K) and CCDW (100 K) phases vs. frequency 46

2.7 Ratio of 100 K 1T-TaS_2 reflectivity to 295 K reflectivity with polarizer in place vs. frequency ... 47

2.8 Reflectivity of 1T-$TaSe_2$ in the CCDW phase 48

2.9 Cavity transmission ratio, $I(TaSe_2)/I(brass)$, vs. frequency at various temperatures 49

3.1 Optical conductivity of 1T-TaS_2 at 100 K calculated from a Kramers-Kronig analysis 64

3.2 Oscillator fit to 1T-TaS_2 reflectivity at 100 K 65

3.3 Oscillator fit to 1T-$TaSe_2$ reflectivity at 295 K 66

3.4 Oscillator fits to 1T-$TaSe_2$ reflectivity at 100 K 67

3.5 Single oscillator fit to 1T-$TaSe_2$ reflectivity at 4.2 K 68

3.6 Oscillator fit to 1T-$TaSe_2$ reflectivity at 4.2 K using two Drude terms 69

3.7 Theoretical cavity transmission ratio for 1T-$TaSe_2$ ... 70

4.1 Basal plane of reciprocal superlattice of CCDW phase . 92

Chapter 1. Introduction

From almost any viewpoint, the transition metal dichalcogenides are interesting materials. Most of these crystals cleave easily along a preferred direction immediately demonstrating their anisotropic, almost two-dimensional character. Wilson and Yoffe (1969) have published an exhaustive description of the structural, optical, and electrical properties of these materials. Many unusual properties in the metallic species were later found to arise from the formation of charge density waves (CDW). Wilson et al. (1975) have given a comprehensive discussion of this phenomenon.

This thesis contains direct evidence of the periodic structural distortion (PSD) caused by the CDW in 1T-TaS_2 and 1T-$TaSe_2$. The large number of phonon modes observed spectroscopically in both crystals is inconsistent with the three atom CdI_2-type unit cell of the host lattice. This implies the formation of a larger unit cell by the CDW-induced PSD. The following discussion will concentrate on the structural and electrical properties of 1T-TaS_2 and 1T-$TaSe_2$. Other work relevant to the CDW-PSD and IR and Raman spectra of these materials will be discussed.

A. Structure of CDW's in 1T-TaS_2 and 1T-$TaSe_2$

DiSalvo and Rice (1979) have given a simple description of CDW's in the transition metal compounds. A CDW is a periodic modulation of the electron density of a crystal over dimensions larger than a unit cell, $\rho(\vec{r}) = \rho_o(\vec{r})(1+ \rho_1 \cos(\vec{q}\cdot\vec{r}+\phi))$. ρ_1, $\vec{q}$, and ϕ are the amplitude, wavevector and phase of the CDW respectively. $\vec{q}$ may or may not be a rational reciprocal of the reciprocal lattice vectors of the host lattice. If it is, the CDW is said to be commensurate (CCDW). If not, it is said to be incommensurate (ICDW).

In the absence of the small (~7%) PSD caused by the CDW's, 1T-TaS_2 and 1T-$TaSe_2$ would have the CdI_2 structure with one molecular unit of three atoms per unit cell. The Ta atom is octahedrally coordinated, six anions being equidistant from it at the corners of an octahedron.

Ta-Ta distances (a_o) and X-X distances (a) are equal; X=S or Se. The Ta-X bond length B_o is not usually determined experimentally and is calculated from the theoretical $a/\sqrt{2}$. c_o is the repeat distance along the c-axis perpendicular to the planes. The values in Table 1.1 are taken from Wilson and Yoffe (1969) and Lucovsky et al. (1973).

The space group of this structure is D_{3d}^3 in the

Schönflies notation. The structure is best described as being hcp S or Se with the smaller Ta ion hexagonally packed in every other layer.

There is no "normal" or undistorted phase in the 1T polytypes of these compounds except at the high growth temperatures ($T > 1200$ K) (Wilson et al. 1975). Careful examination of the X-ray, electron, and neutron diffraction patterns reveals deviations from the exact CdI_2 structure at all temperatures below 600 K. Weak satellite spots imply a superlattice distortion whose wavevector is $\vec{q}=\vec{a}^*/\sqrt{13}$, where $\vec{a}^*$ is the basal plane reciprocal lattice vector of the undistorted phase. Below 180 K in 1T-TaS_2 and 473 K in 1T-$TaSe_2$, the superlattice is commensurate with the host CdI_2 lattice, and $\vec{q}=\vec{a}^*/\sqrt{13}$ in the commensurate CCDW state. Above 370 K in 1T-TaS_2 and 473 K in 1T-$TaSe_2$, the distortion wavevector increases by $\sim 2\%$ and rotates slightly so that the superlattice is incommensurate with the host lattice (ICDW). Between 220 K and 350 K in 1T-TaS_2 a unique "quasicommensurate" (QCDW) phase exists intermediate to the other two states. In this phase, the CDW stops just short of becoming commensurate. As the temperature is increased in the ICDW phase of both compounds, an irreversible transition to the 2H or 3R polytypes takes place before an undistorted phase can be reached.

As it is the CCDW phase that is of most interest to this work, it is worth discussing in some detail. It should be mentioned that the space group of the CCDW phase of 1T-TaS_2 and 1T-$TaSe_2$ has never been reported, probably due to the difficulty of analyzing the weak diffraction spots of the anions.

It is presently accepted that in both 1T-TaS_2 and 1T-$TaSe_2$, a $\sqrt{13}$ x$\sqrt{13}$ a unit cell is formed in the basal plane. Fig. 1.1 shows the basal plane of Ta atoms and unit vectors of the unit cell. Also shown are the unit vectors of the triple-axis CDW distortion in the basal plane of the crystal. (Scruby et al. 1975, Moncton et al. 1975). The CDW stacking is such that each successive layer is shifted so as to move the CDW charge extrema as far apart as possible.(Moncton et al. 1976). This leads to a triclinic unit cell with 39 atoms per unit cell. The stacking is such that an equivalent CDW site is found every 13 c_o cell units along the c-axis. The space group of the superlattice has not been reported. It is also not clear whether the CDW-PSD wavevector has a component out of the basal plane.

The detailed changes to the 1T-TaS_2 lattice caused by the CCDW have been discussed by Wilson (1978a). The Ta-Ta separation in the star surrounding the cell corners has been reduced by up to 6.5%. Site a has had about one electronic charge added to it. Site b has had only a small amount of

charge added to it while site c has had about 0.4 e taken from it. The anions are not affected as much.

As the displacements and charge transfers are significant, the band structure must be somewhat modified in its transfer to a smaller Brillouin zone . The interatomic force constants and effective charge must also be affected, changing the phonon spectrum. The details have never been worked out, not surprisingly in view of the difficulty of even the simplest model calculation.

B. Electrical conductivity

The effect of CDW formation on the band structure is clearly demonstrated by the behavior of the DC resistivity. Fig. 1.2 (Wilson et al. 1975) shows $\rho(T)$ along the layers for typical crystals of 1T-TaS_2 and 1T-$TaSe_2$. $\rho(T)$ along the c-axis has not been reported.

At all the temperatures where diffraction results show structural transitions taking place, the resistivity also changes abruptly. Except for the CCDW (low temperature) phase of 1T-TaS_2, the observed values are characteristic of a poor metal. The magnitude of the resistivity of 1T-TaS_2 in the low temperature CCDW phase is characteristic of a semiconductor. However, a single gap model will not fit the data over the

entire temperature range.(Tidman and Frindt 1976). Fazekas and Tossati (1979) have discussed this temperature dependence in terms of Mott localization.

For this work, the significance of the DC electrical resistivity lies in its implication for the optical conductivity in the far-infrared. It will be seen that phonon modes are heavily screened in both materials except in the CCDW phase of 1T-TaS_2.

C. Phonons in other transition metal dichalcogenides.

1. Optical studies.

The wavelength of optical radiation used to probe the phonon excitations of a solid is large compared with the range of wavelengths of the phonons. As a result, for first order processes involving the destruction of a photon and the creation of a phonon, only long wavelength k=0 phonons can take part. The methods of group theory provide the most powerful tool for understanding the vibrations in a crystal lattice. At k=0, the vibrations have the symmetry of the point group of the crystal. Γ, the reducible group of lattice vibrations, can be decomposed into its irreducible representations using character tables of the point groups, orthogonality relations, and the symmetry of each atom in the unit cell, as obtained from diffraction data

(Fateley et al. 1972). This method is far easier than finding the normal modes by diagonalizing a large matrix. However only the number of phonon modes and their symmetries are determined, not their frequencies.

CdI_2 is the obvious example. Since there are three atoms per unit cell, there are 3n=9 normal modes. A 9x9 matrix would have to be diagonalized to find them directly. CdI_2 has the D_{3d} point group and D_{3d}^3 space group. The site symmetry of each atom can be found in Wyckoff (1963). The correlation method described by Fateley et al. (1972) can then be used to reduce Γ.

The result can be expressed as follows.

$$\Gamma = A_{1g} + E_g + 2A_{2u} + 2E_u .$$

The A's are one dimensional representations and are associated with displacements along the c-axis. The E's are two dimensional representations associated with displacements in the basal plane. The E modes are two-fold degenerate, as expected for a uniaxial crystal.

For point groups with inversion symmetry, such as D_{3d}^3, the representations have a subscript u or g denoting whether displacements have odd or even parity. (cf. ungerade, gerade in

German). In such groups IR modes have the odd parity associated with a dipole moment, while Raman modes do not. IR or Raman activity is usually given in the character table.

Three modes must be the acoustic modes associated with a translation of the entire lattice which must have odd parity. This is written $\Gamma_{acoustic}=A_{2u}+E_u$. The remaining 3n-3 modes must be optic and this is expressed as $\Gamma_{optic}=A_{1g}+E_g+A_{2u}+E_u$. The first two represent Raman modes, the second two IR modes. Using matrix representations and performing the symmetry operations on small displacements from equilibrium, the form of the normal coordinates can be found. This has been done for the CdI_2 structure (Lockwood 1969), and is described in Fig. 1.3a.

For future reference, it is useful to mention the 2H polytype. Wieting and Verble (1971) have worked out this case. In this structure the cations are trigonally coordinated. There are two formula units and two layers in the unit cell. With six atoms per unit cell, there are 18 phonon modes or branches in the phonon spectrum.

Γ-point (k=0) decomposition yields the following expression.

$$\Gamma=2A_{2u}+B_{2g}^{1}+B_{2g}^{2}+B_{1u}+A_{1g}+2E_{1u}+E_{2g}^{1}+E_{2g}^{2}+E_{2u}+E_{1g}$$

The B modes are optically inactive and one A_{2u} and E_{1u} mode are acoustic. This leaves two IR modes, A_{2u} and E_{1u}, and four Raman modes, $E_{2g}{}^1$, $E_{2g}{}^2$, E_{1g}, and A_{1g}. The ion motion is pictured in Fig. 1.3b.

The forces between layers, anion-anion bonds, are much weaker than forces within the layers, Referring to Fig. 1.3, in such a case, the $E_g(A_{1g})$ and $E_{1g}(A_{1g})$ modes of the 1T and 2H structures would be expected to have similar frequencies. A similar argument would apply to the IR modes $E_u(A_{2u})$ and $E_{1u}(A_{2u})$. That is, the vibrations in both these crystals are closely related due to weak interlayer coupling.

Of the additional optic modes appearing in the 2H structure, the $E_{2g}{}^2$ is similar to an acoustic mode and should have a low frequency. It is called a "rigid-layer mode". The $E_{2g}{}^1$ mode is similar to the E_{1u} optic mode and could be expected to have a similar frequency.

Table 1.2 summarizes the experimentally observed optical frequencies known at the time of writing for the compounds listed. 1T-TaS_2 and 1T-$TaSe_2$ do not have a normal or undistorted phase and are not included. They are the subject of

this thesis and will be discussed later. Not much work has been done on the tellurides, perhaps because the structure of many of them is distorted (Wilson 1969), or they are hard to grow.

The very small change a phonon resonance causes in the high infrared reflectivity of a metal is difficult to detect. "met" in the table means that the electrical conductivity is characteristic of a metal and that this mode will likely be difficult to detect. More Raman data are available because results can be obtained from metals. Experiments are difficult due to small penetration and weak signals but can be done.

Determination of the A_{1u} IR mode requires incident radiation with the electric field along the direction of vibration. These crystals generally grow in the form of thin platelets less than a millimeter thick. It is difficult to prepare a specimen with a smooth surface parallel to the c-axis. Even pressed powder samples exhibit a high degree (90%) of orientation (Lucovsky et al. 1973). As a result, the A_{1u} mode has not been determined for most of these crystals.

The binding in these compounds can be either ionic, covalent, or metallic. Lucovsky et al. (1973) have looked at the differences between the group IVB compounds ZrS_2, HfS_2, and $HfSe_2$ and the group VIB compounds MoS_2, $MoSe_2$, WS_2, and WSe_2. These compounds are not metallic and have readily

observable IR modes. Large transverse-longitudinal mode frequency splitting suggests ionic bonding. For example for HfS_2 $\bar{\nu}_{TO}$= 166 cm^{-1}, $\bar{\nu}_{LO}$=318 cm^{-1}. The much smaller splitting in the group VIB compounds ($MoSe_2$=3cm^{-1}) suggests covalent bonding. Comparison of the bare ionic radii with the observed lattice spacing gives more evidence that in the group IV compounds, the bonding is ionic, while in the group VI compounds it is covalent. $ZrTe_2$ and $HfTe_2$ were found to be metallic.

Simple models have been used to describe the optic modes observed in 2H-MoS_2. Bromley (1971) used the Born-von Karman model in the nearest-neighbor approximation considering only a single layer. Force constants were determined from a couple of experimentally observed modes. The model then predicted the other modes fairly well. Of course this model does not predict the $E_{2g}{}^2$ rigid-layer mode or the $E_{2g}{}^1$ mode which result from two layers in a unit cell.

Wieting (1973) applied a simple linear-chain model to both 2H-MoS_2 and GaSe. Using the symmetry considerations leading to the mode motion depicted in Fig. 1.3, each mode in the model is easily solved. Force constants determined by a fit to one experimental mode predicted the frequency of another fairly well. From the near degeneracy of the E_{1u} and $E_{2g}{}^1$ mode frequencies, he concluded that the S-S interlayer binding was

weak. This justifies Bromley's neglect of this interaction.

2. Neutron diffraction studies.

Inelastic neutron diffraction can be the best method of studying phonons because it is not restriced to k=0 as are first order optical studies. The end result is a complete phonon dispersion curve. However the small volume of available transition metal dichalcogenides crystals makes this determination difficult.

Among the transition metal dichalcogenides, only for 2H-MoS_2 has the complete phonon spectrum been determined. Wakabayashi et al. (1975) used a sample 13x8x0.2 cc, very large for this class of crystals. A simple shell model lattice dynamical calculation with a polarizable Mo atom gave fair agreement with experiment. At the k=0 Γ-point, experimental frequencies agreed with those of Wieting and Verble (1971).

2H-PbI_2 has also been completely studied by Doerner et al. (1976). This has the CdI_2 structure but has the 2H prefix in the literature, referring to two hexagonal iodine planes in the unit cell. Their k=0 phonons agreed with optical measurements.

The above study is particularly interesting because the

Raman modes were also determined for the 4H polytype. This has double the height and number of atoms in the unit cell. This causes the A point at the edge of the 2H Brillouin zone to be folded back to the k=0 Γ-point of the 4H Brillouin zone. An additional Raman mode appears in the 4H structure at a similar frequency to an acoustic mode at the zone edge (A) of the 2H crystal. This phenomenon will be seen to occur for transition metal dichalcogenides where a CDW-PSD enlarges the unit cell by forming a commensurate superlattice. Additional work on PbI_2 has been done by Sears et al. (1979).

Moncton et al. (1977). found that the LA phonon branches along the Γ-M direction in 2H-$TaSe_2$ went to 99 cm^{-1} at the zone edge. Also the Γ- point $E_{2g}{}^2$ frequency was found to be 24 cm^{-1}. This is in excellent agreement with the Raman frequency determined by Holy et al. (1976) and Steigmeier et al. (1976). The neutron work did not extend past 120 cm^{-1} and thus missed most of the optic branches. They also studied 2H-$NbSe_2$ where the $E_{2g}{}^2$ mode frequency agreed with the Raman work of Wang and Chen (1974).

There has been a great deal of interest in studying the softening of the LA phonon branch at a wavevector spanning the Fermi surface, known as a Kohn anomaly. (Ziman 1969) The amount of softening is a measure of the electron-phonon coupling.

A Kohn anomaly has been seen at room temperature in the QCDW phase of 1T-TaS_2 by Ziebeck et al. (1977). It occurred at approximately the wavevector of the CDW distortion observed in diffraction. That is $q \cong a_o^*/\sqrt{13}$.

Moncton et al. (1975) have observed Kohn anomalies in both 2H-$TaSe_2$ and $NbSe_2$ at $q \cong a_o^*/3$. The frequency of the mode softened as the $TaSe_2$ entered into its CCDW phase phase at 123 K, but not completely to zero.

No Kohn anomaly was seen in 1T-$TiSe_2$ by Stirling et al. (1976). This was to be expected as a group IV compound does not have the extra electron of the group V compounds. However this work was done at room temperature, while the CCDW distortion does not set in until 200 K.

In summary, a large Kohn anomaly often appears in materials with CDW distortions and indicates a strong electron-phonon coupling. Neutron data is limited to only a few compounds and even then only the acoustic branches were determined. All the authors commented on the difficulty of working with small crystals.

D. Phonons and CDW's. Far-infrared and Raman studies.

Many groups have studied phonons in compounds sustaining

CDW distortions using far-infrared and Raman spectroscopy. In cases where a commensurate superlattice is formed, the increased number of molecules per unit cell increases the number of optic modes. In ICDW phases extra Raman lines often appear. The Raman modes appear to be more strongly coupled to the CDW than the infrared modes as implied by their temperature dependence near the CDW phase transitions.

The following is a brief summary of the work done so far in this field. The discussion is by compound, down and then across the periodic table. Raman work is reported first.

Holy et al. (1977) have studied 1T-$TiSe_2$ using both Raman and far-infrared spectroscopy. They observed far more phonon modes than group theory would predict for an undistorted lattice when the $TiSe_2$ was in its CCDW state below 200 K. From the known form of the superlattice, they predicted both the number and symmetry of the modes folded in to k=0 from the undistorted Brillouin zone. Most of the observed modes were satisfactorily explained in this way. Some of the modes displayed temperature dependence, the Raman more than the IR modes. This is not understood very well at present but is presumed to be due to phonon coupling to the CDW.

Liang et al. (1979) have observed similar mode multiplicity in the CCDW phase of 1T-$TiSe_2$. Their phonon work concentrated

mainly on the temperature dependence of their phonon spectra. The results suggested an antiferroelectric transformation at the 200 K CDW onset temperature. They proposed a model of the CDW phase transition driven by the phonons.

Wilson et al. (1978b) have also seen mode multiplicity in the CCDW phase of 1T-$TiSe_2$. This work concerned itself more with the effect of the CDW on the band structure and free carriers than on the phonon properties.

Smith et al. (1976) found just one Raman mode in room temperature 1T-VSe_2. However, at 2 K at least five additional modes appeared implying the formation of a superlattice. A detailed analysis of any temperature dependence was not given.

Tsang et al. (1976) have also seen Raman modes in the ICDW phase of 2H-$NbSe_2$. Two weak low frequency lines appear below the transition temperature of 33.5 K. A broad line at the lowest frequency softens completely to zero at the transition. It is identified with an amplitude mode of the CDW and follows the temperature dependence predicted by Rice and Strassler (1974).

Duffey et al. (1976)have observed more than thirty Raman modes in the CCDW phase of 1T-TaS_2. Most of their peaks were attributed to the formation of a superlattice, but some seemed related to CDW-phonon coupling. Similar, but less detailed,

spectra were observed by Smith et al. (1976). Holy (1978) also determined the Raman spectrum of 1T-TaS_2. Only in the determination of weaker modes do the two workers disagree.

Sai-Halasz and Perry (1977) have studied the low frequency (< 150 cm^{-1}) Raman modes of 1T-TaS_2. The strongest mode at 82 cm^{-1} showed unusual behavior with both temperature and polarization. They speculated that this was a phase mode of the CDW.

Tsang et al. (1977) have studied the Raman spectrum of 1T-$TaSe_2$. They found an increase in the number of modes upon cooling to the CCDW phase. Some lines changed very little in frequency or intensity, while others seemed strongly coupled to the CDW, softening and strengthening considerably at lower temperature. Several speculations on the nature of this interaction were put forth.

Holy et al. (1976) and Steigmeier et al. (1976) have studied 2H-$TaSe_2$ using Raman spectroscopy. Steigmeier et al. fitted the Raman modes to Lorentzian line shapes and deduced which ones were strongly coupled to the CDW excitations from their temperature dependence. Holy et al. went further and discussed a theory which could account for the results by interaction of a longitudinal phonon branch with the CDW.

Lucovsky et al. (1976) reported a single weak IR mode at 210 cm^{-1} in the QCDW phase of 1T-TaS_2. At room temperature they saw six IR modes in the CCDW phase of 1T-$TaSe_2$, evidence of a large unit cell. Karecki and Clayman (1976,1979) have seen ten strong IR modes in the CCDW phase of both these crystals. This work forms the basis of the experimental part of this thesis.

In conclusion, there appears to be a fair amount of interest in the phonon modes folded in to k=0 by CDW-PSD's. Of particular interest is the coupling of these modes to the CDW itself. This has been seen in the softening of certain Raman modes. Modes which disappear at the transition out of the CDW phases have been interpreted as either amplitude or phase modes of the CDW itself.

In the next chapter details of sample preparation and measurement technique are presented. Chapter 3 describes how the reflectivity spectra were analyzed using oscillator fits and the Kramers-Krönig relations. Chapters 4 and 5 discuss the interpretation of the reflectivity spectra in terms of phonons and plasmons (free carrier excitations). A summary of the significant findings of this study is given in the final chapter.

Table 1.1

Lattice parameters of 1T-TaS_2 and 1T-$TaSe_2$ in nm.

	a_o	c_o	B_o
1T-TaS_2	0.3346	0.5859	0.2366
1T-$TaSe_2$	0.3477	0.6273	0.2459

Table 1.2. Optical phonon frequencies in wavenumbers for some transition metal dichalcogenides.

	A_{1u}	E_u	E^2_{2g}	E^1_{2g}	A_{1g}	E_g
1T octahedral coordination						
TiS_2		175[11]			335[5]	232[5]
$TiSe_2$		137[10] 144[11]			195[5]	134[5]
ZrS_2		181[12]			333[5]	235[5]
$ZrSe_2$		128[13]			194[5]	148[5]
HfS_2		166[12]			337[5]	253[5]
$HfSe_2$		98[12]			198[5]	155[5]
VSe_2		met.[15]			206[4]	
2H trigonal prismatic coordination						
$NbSe_2$		met.[13]	30[3]	237[2] 238[3]	230[2] 231[3]	133[18]
TaS_2		met.[16]	25[17]	285[17]	399[17]	203[17]
$TaSe_2$		met.[14]	23[8] 25[9]	207[2,8]	234[2,8]	139[8] 2LA?[2]
MoS_2	470[6,12]	377[1] 384[6,12]	34[7]	377[1] 383[6]	395[1] 409[6]	298[1] 287[6]
$MoSe_2$	350[12]	283[1] 288[12]		285[1]	361[1]	217[1]
$MoTe_2$		240[1]		237[1]	321[1]	201[1]
WS_2	435[12]	356[12]				
WSe_2	305[12]	245[12]	25[14]	250[14]	253[14]	178[14]

Table of superscripts on next page.

Table 1.2(continued). List of superscripts.

1. Agnihotri et al. (1973)
2. Tsang et al. (1978)
3. Wang and Chen (1974)
4. Smith et al. (1976)
5. Nathan et al. (1972). Smith et al. (1972)
6. Wieting and Verble (1971)
7. Verble and Wieting (1971)
8. Holy et al. (1976)
9. Steigmeier et al. (1976)
10. Holy et al. (1977)
11. Lucovsky et al. (1976)
12. Lucovsky et al. (1973)
13. Karecki (1975)
14. Mead and Irwin (1977)
15. Bayard and Sienko (1976)
16. Wilson et al. (1975)
17. Klein et al. (1976)
18. Duffey (1978)

Figure 1.1

a) CdI_2 unit cell in basal plane.

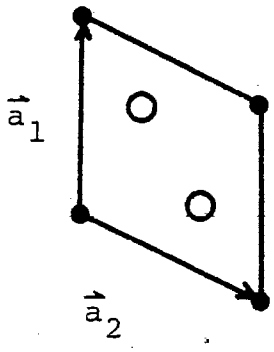

$\vec{a}_1 = a\,\hat{j}$

$\vec{a}_2 = (\sqrt{3}/2)a\,\hat{i} - a/2\,\hat{j}$

$\vec{a}_3 = c\,\hat{k}$

Ta at (0,0,0)

S or Se at (1/3,2/3,u)
(2/3,1/3,-u)
u=1/4

b) commensurate unit cell showing only cations.

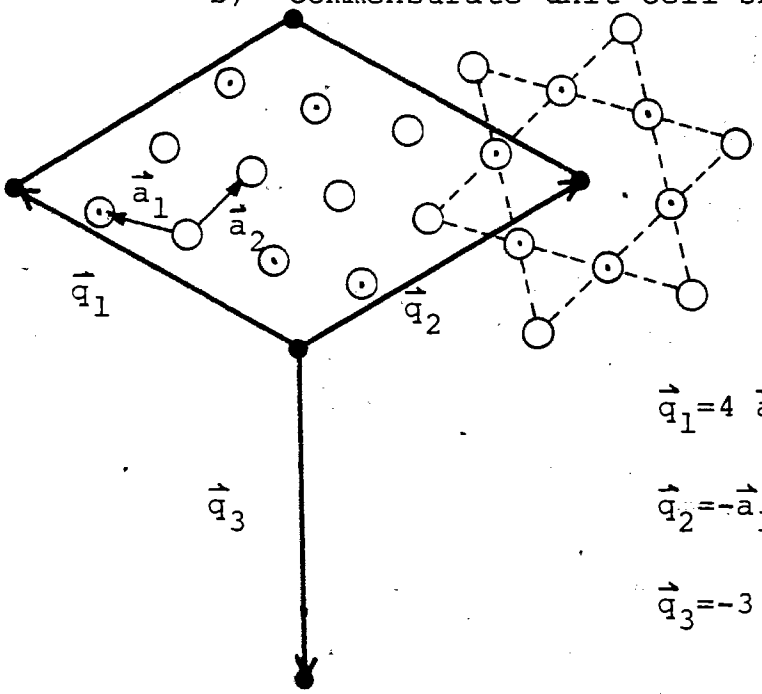

● corner, type a.
⊙ type b
○ type c

$\vec{q}_1 = 4\,\vec{a}_1 + \vec{a}_2$

$\vec{q}_2 = -\vec{a}_1 + 3\,\vec{a}_2$

$\vec{q}_3 = -3\,\vec{a}_1 - 4\,\vec{a}_2$

Figure 1.2.

Resistivity vs. temperature for 1T-TaS_2 and 1T-$TaSe_2$ taken from Wilson et al. (1975).

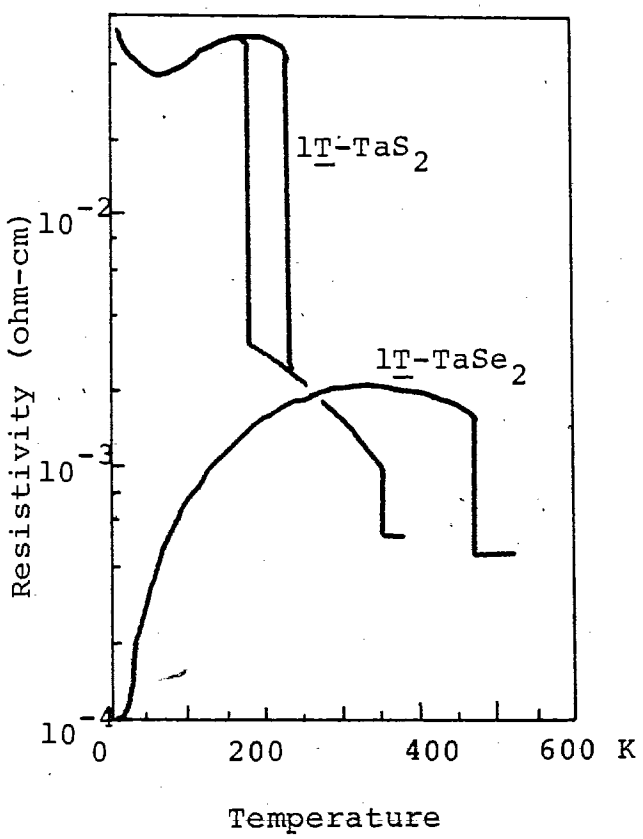

Figure 1.3

Normal modes of the 1T and 2H structures.

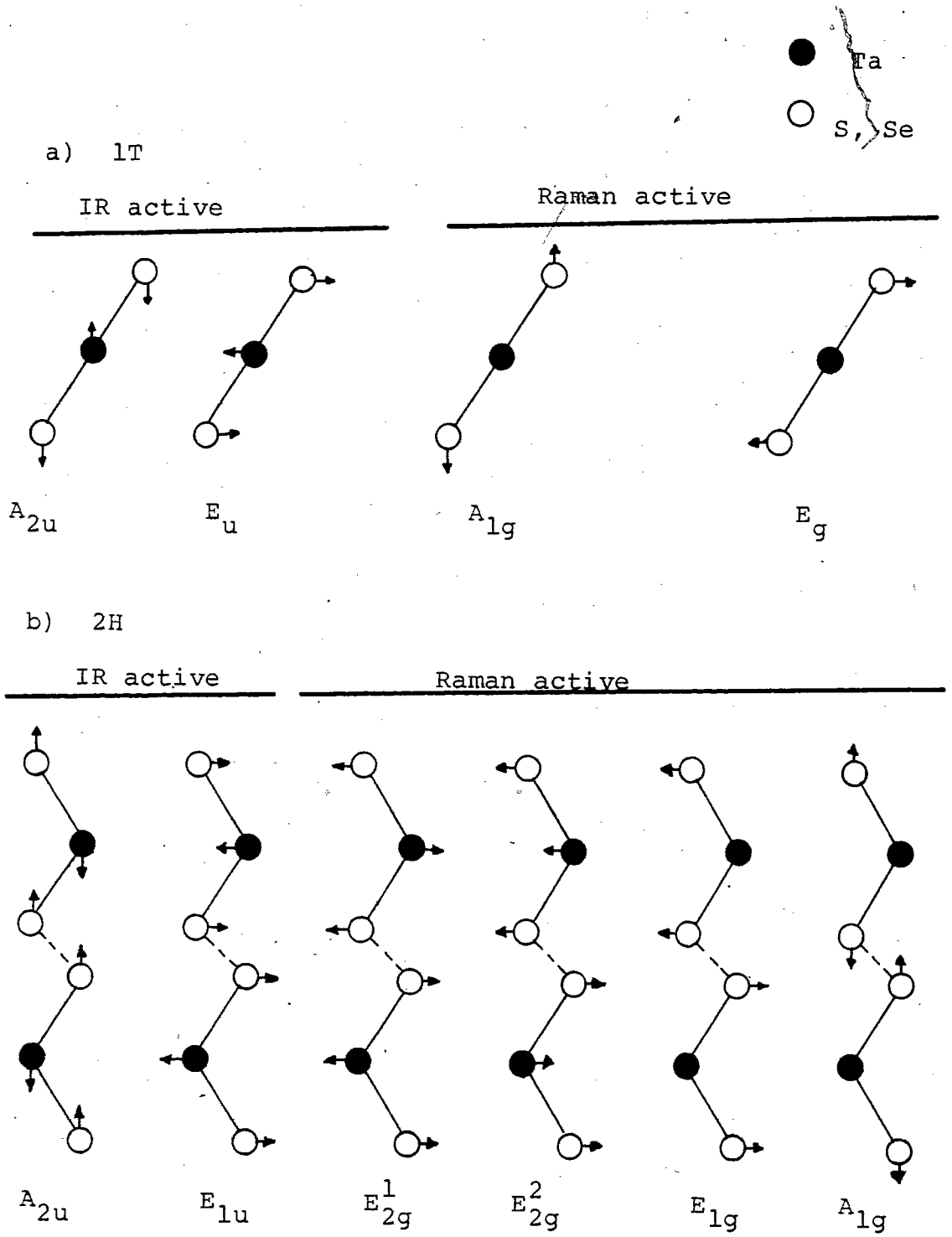

Chapter 2. Experiment

A. Crystal growth.

Both 1T-TaS_2 and 1T-$TaSe_2$ crystals were grown by the iodine vapor transport method. The 1T-TaS_2 crystals were provided by J. P. Tidman. The 1T-$TaSe_2$ crystals were grown by the author especially for this experiment. The details of the crystal preparation follow.

Stoichiometric amounts of Ta and Se (3.5 g total) were placed in a cylindrical quartz-glass tube (2x28cm). Enough excess Se and I_2 were added to give about 1 atm pressure at 950 C. The excess Se was added to ensure proper stoichiometry.

The tube was heated to 600 C for two days. This was followed by a back transfer with one end of the tube at 1000 C, the other at 925 C. This ensured that all reagents went to the cool side, leaving no nucleation centers in the growth zone.

The temperature gradient was then reversed for ten days. This temperature is 25 C cooler than that reported by DiSalvo et al. (1974) and was found to be crucial for results. The tube was taken directly from the furnace and plunged into ice cold water to quench the crystals into the metastable 1T phase. The iodine is responsible for much of the heat transfer during the

quench.

One very large crystal ~2x1cm resulted, along with many smaller ones. They were gold in color with good optical surfaces. The 1T-TaS_2 crystals were also gold. No direct tests of stoichiometry were performed but an indirect measure can be obtained from resistivity measurements.

B. Resistivity measurements.

In order to characterize the particular samples used in these experiments, the resistivity, $\rho(T)$, was measured using Van der Pauw (1958) geometry. This is a four-probe technique where the sample must be of known thickness. Errors arise from the size of the contacts, assumed to be points. "Crystalbond 509" held the sample to a Cu substrate. The contacts were made with a silver paint. The results are plotted in Fig. 2.1.

The absolute value of the resistivity of 1T-TaS_2 obtained were at wide variance with those reported in the literature. Evidently the sample was either not of uniform thickness or the weight, about 2 mg, was not determined accurately. At room temperature, other observers report resistivities in the range $8\text{-}10X10^{-4}$ohm-cm. (Tidman and Frindt 1976. Thompson et al. 1971. DiSalvo and Graebner 1977). The variations between crystals is most evident in the widths of the QCDW-CCDW

transition and the low temperature resistivities. The relative results obtained here were normalized to $9X10^{-4}$ohm-cm at room temperature.

The 1T-$TaSe_2$ crystal used was thicker and more uniform than the 1T-TaS_2 crystals used above. Its thickness was determined by weight, estimated surface area, and density obtained from lattice parameters. Finite contact size and the area determination combine to give an estimated 10% error. The results are plotted in Fig. 2.2.

The 1T-$TaSe_2$ ICDW-CCDW transition occurred at the established value of 473 K with a 12 K hysteresis as measured in a separate experiment. The crystal used was from the same batch as that used to determine the absolute resistivity between 295 and 4.2 K. It is reasonable to assume that their room temperature resisitivities are comparable. This gives $\rho(473\ K)=4X10^{-4}$ ohm-cm for the resisitivity directly above the QCDW-ICDW transition.

C. Reflectivity measurements.

Almost all the spectra were obtained using Fourier transform spectroscopy. This technique is well established. Chantry (1971) has given a good elementary exposition. Light from a broadband light source is split into two paths either by

amplitude division (Michelson interferometer) or by wavefront division (lamellar interferometer). One path length is fixed, the other can be varied. At zero-path difference, light of all frequencies will interfere constructively. As one path length is varied, light of different frequencies will interfere, some constructively, others destructively when the two beams are recombined. Recording the intensity versus path difference of the combined beam produces an interferogram. Placing a sample into the beam permits spectroscopy to be performed. Since the interferogram is the Fourier transform of intensity versus frequency, it can be inverted by computer to yield a spectrum. The advantages of this technique are realized most fully in the far-infrared region of the spectrum ($\bar{\nu} < 250$ cm^{-1}).

Most of the experimental details of the apparatus used here have been discussed by Templeton (1973). As a result, the following description will be brief, emphasizing characteristics responsible for the ultimate signal-to-noise ratio and resolution of the resulting spectra.

1. Light source.

A water cooled quartz jacketed mercury arc supplied the broad band light necessary for Fourier transform spectroscopy. The output of the one used tends to vary occasionally over a period of minutes. These effects are called "lamp

fluctuations". They are random and can be averaged out by averaging either spectra or interferograms.

2. Interferometer.

a. Beckman RIIC FS-720 Michelson interferometer.

An essential part of any Michelson interferometer is a beamsplitter to divide the amplitude of the light source into two paths. In this instrument, they are constructed from thin Mylar films. These make use of thin film interference to divide the beam amplitude. In order of thickness, the 15G, 25G, 50G, and 100G beamsplitters have zero efficiency every 750, 450, 220 and 110 cm^{-1} respectively. Their maximum efficiency is reached midway between the zeroes and can reach 75%.

The path length difference is varied in step-wise fashion and the interferogram is sampled at each step. A result of this periodic sampling is that the calculated spectrum repeats itself every frequency interval of 1/2(step size). Frequencies higher than this cutoff frequency are folded back to lower frequencies, distorting the spectrum. A low pass filter is used to cut off these high frequencies, usually aided by the first minimum of the beamsplitter.

The stepping motor on our FS-720 moves the mirror in steps

of 2.5 microns. The maximum frequency that can be obtained is limited by this to 1000 cm^{-1}. Using this step size, best spectra were obtained with the 15G beamsplitter and a black polyethylene filter. Absorption lines in the Mylar and the rolloff in beamsplitter efficiency towards its first minimum at 750 cm^{-1} restrict the useable bandwidth to 600 cm^{-1} and below.

Since the beamsplitter efficiency goes to zero at zero frequency, there is a lower limit to the useable frequency of a spectrum. Thicker beamsplitters are more efficient at lower frequencies than thinner ones. Thus to obtain a complete spectrum, different beamsplitters and filters must be used. The configurations used in these experiments are listed in Table 2.1. Complete spectra are obtained by splicing together spectra taken with different beamsplitters at frequencies where they overlap.

In Fourier transform spectroscopy the increased number of spectral elements required for higher resolution ($\Delta\bar{\nu}$) is obtained by increasing the path length difference recorded in the interferogram. That is, $\Delta\bar{\nu} \simeq 1/L$, where L is the maximum path length. The maximum resolution used here was 0.5 cm^{-1}, less than the machine's 0.1 cm^{-1} capacity. In practice, the resolution is limited by signal-to-noise since at large path length difference, the variations in signal caused by

interference are obscured by noise.

As the interferogram is recorded, the steps themselves can vary causing random stepping errors which distort the spectrum. As an example of this effect, replacing the sticky grease on the vacuum seal of the moveable mirror made a significant improvement in repeatability. Averaging interferograms or spectra will reduce this error.

b. Beckman RIIC LR-100 Lamellar interferometer.

This instrument uses a special slotted mirror to split the wavefront and introduce a path difference. It is diffraction-limited to a high frequency limit 100 cm^{-1}. Its low frequency limit is determined by waveguide effects in the mirror and is about 2 cm^{-1}. The instrument is most effective below 50 cm^{-1}. It was used primarily below 25 cm^{-1} where it is superior to the FS-720.

3. Detector system.

One detector was a Ga-doped Ge bolometer cooled to near 0.3 K using pumped He^3. In practice, its signal-to-noise ratio was limited by spurious vibrations of the cryostat assembly. That is, noise would come and go, sometimes related to fluid levels. Dampening procedures (rubber mounts,

strategically placed weights) seemed to help, as did varying the light chopping frequency. The less signal, encountered in using the lamellar interferometer or absorbing samples, the worse the signal-to-noise. Longer measurement time at each point is effective with this kind of noise.

The sample section of the cryostat consisted of a 5 cm diameter tube about one meter long. This isolates the light path to the detector from the surrounding liquid He. This tube is large enough to accomodate a variety of sample configurations at low temperatures. A dual cavity and 15° single reflection apparatus could fit into this sample tube.

The quartz window isolating one He^3 system absorbs freqencies higher than 330 cm^{-1}. The mylar window in the other detector cryostat has annoying absorption lines above 500 cm^{-1}. To obtain spectra to 600 cm^{-1}, a doped Ge bolometer that fit into a liquid He storage dewar was used. Its signal-to-noise is inferior to that of the 0.3 K system, restricting useable resolution to 2 cm^{-1} even with averaging.

4. Sample configuration.

All light was directed from the interferometer to the sample and then to the detector using 13mm dia. light pipes. These were tubes of either polished brass or gold-coated

stainless steel. Two types of sample configurations were used, single bounce or multireflection. For temperatures below 80 K, the samples were mounted inside the sample tube of the detector cryostat. Above this temperature, the samples were mounted outside, in a separate cryostat.

a. Single bounce.

(1). Near normal incidence.

Low temperatures, T ~ 4.2 K, were obtained by placing the sample into the sample tube of the detector cryostat. Fig. 2.3 shows the sample holder. The sample chamber is cooled only with exchange gas coupling to the outer He bath. The reference was polished brass and was mechanically rotated into the beam from outside the detector cryostat.

To go above 80 K, a simple optical dewar was placed into the beam outside the detector cryostat and interferometer. Windows were of polyethylene. Fig. 2.4a is a schematic diagram of the arrangement.

The 1T-TaS_2 crystals used were small, necessitating the use of a composite sample. Here, Al foil pressed over the sample served as a reference. Al is a good metal and highly reflecting in the far-infrared.

A single, large (2x1.2 cm^2) 1T-$TaSe_2$ crystal was used. The surface was of good optical quality. This permitted polished brass to be used as a reference.

(2). 45° incidence.

This configuration was used to gain information about polarization dependence of the reflectivity. A schematic diagram of the experimental setup is shown in Fig. 2.4b. The polarizer is a mylar film on which 500 lines per inch of gold is evaporated. As the grating spacing is much less than far-infrared wavelengths, radiation polarized perpendicular to the grating is transmitted virtually unattenuated. The other component is strongly reflected.

b. Multireflection.

To bring out weak structure, crystals were placed into non-resonant cavities (Ward 1976). See Fig. 2.5. The light from the interferometer is spread out by conical light cones so as to make many bounces before exiting to the detector. The number of bounces made is a function of the cavity's reflectivity. It can range from hundreds in the case of a very reflecting cavity to one for highly absorbing samples.

For high temperature runs ($T > 400$ K), a single cavity was used. The reference spectra were taken with the bare cavity before heating. Many crystals were attached to the cavity walls. Mechanical clips were used to hold the crystals at the higher temperatures in order to avoid contamination from any adhesive. At lower temperatures, ($T < 400$ K), the dual cavity was used for the convenience of taking a reference spectrum. Samples were held in with Crystalbond adhesive. It was difficult to align the apparatus. Runs taken on different days sometimes disagreed with one another in absolute values by up to 25%.

6. Fourier transforms.

Interferograms with up to 512 points were transformed on an HP2115A minicomputer. The Fourier transform programs were written by Templeton (1973), David Pappi, or Brian Farnworth. The reflectivity spectra were obtained by digital division of sample and reference spectra.

7. Grating spectra.

Some room temperature measurements were taken with a Perkin-Elmer 457 grating spectrometer using a Beckman C-621 beam condenser and MSP-02 reflectance attachment. This extends from 250 on up to 4000 cm^{-1}. Since the beam is condensed to a

smaller size it was used to get an absolute reflectivity measurement on small crystals. The spectra could then be compared with those taken on the inteferometers.

D. Far-infrared reflection spectra results.

Spectra were taken in all phases of both 1T-TaS_2 and 1T-$TaSe_2$ crystals.

1. 1T-TaS_2 spectra.

a. ICDW phase. T > 370K.

Single reflection spectra taken at 390 K were featureless, the reflectivity dropping off slightly at higher frequencies. The absolute value could not be determined sufficiently accurately to detect any deviation from the Hagen-Rubens relation (Ziman 1969). That is, typical metallic reflectivity was observed below 500 cm^{-1}. It was not felt that averaging would increase the signal-to-noise enough to observe any phonon modes, especially since none was seen in the QCDW phase.

b. QCDW phase. 220 K < T < 350 K.

A four percent decrease in integrated intensity was

observed over the range 0-500 cm^{-1} as the crystal was cooled below 358 K. The spectrum had a peak frequency near 200 cm^{-1}. At room temperature the reflectivity was found to be featureless, typical of a metal, and adequately described by the Hagen-Rubens relation. Putting the crystals in the multireflection cavity did not bring out any weak structure. A typical spectrum is shown in Fig. 2.6. 100 cm^{-1} is the splice point of two spectra taken with filter and beamsplitter combinations appropriate for higher and lower frequencies. The drop in beamsplitter efficiency at this point makes the spectra noisy. An experiment to fill in this frequency range was not considered to be worth the effort. Three points calculated fom the Hagen-Rubens relation (3.6) are indicated in Fig. 2.6.

c. CCDW phase. $T < 180$ K.

Under the same conditions as above, the integrated intensity dropped another 15% at the QCDW-CCDW transition. Many reststrahlung-like peaks appeared, and little temperature dependence of these peaks was noted. The complete spectrum at 100 K is shown in Fig. 2.6. It is constructed from spectra taken with three different beamsplitter-filter combinations.

At 45° incidence, some data were taken with polarized incident light. For p-polarization, the low frequency modes (50-120 cm^{-1}) were stronger than for s-polarization. The high

frequency modes were polarization independent. Fig. 2.7 shows the ratio of reflectivity at 100 K to 295 K with polarizer in place. One high frequency mode at 204 cm^{-1} is also shown to demonstrate that it is polarization independent. Since it occurs close to the cutoff frequency where the intensity is low, the fact that the ratio seems to be greater than one is of no concern. In fact, the results are very good for being so close to the cutoff frequency.

2. 1T-$TaSe_2$ spectra.

a. Cavity spectra. ICDW and CCDW phases. $500 > T > 295$ K.

Spectra were taken with the single cavity. At room temperature, multiple phonon modes appeared. (see below). As the temperature was raised to 500 K, the integrated intensity increased by 10% for $\bar{\nu}_{peak}$=100 cm^{-1} and 6% for $\bar{\nu}_{peak}$=60 cm^{-1}. All structure disappeared to within 1% signal-to-noise. It reappeared upon cooling.

b. Single reflection spectra. CCDW phase. $T \simeq 295$ K.

Spectra taken at 15° incidence are presented in Fig. 2.8. Spectra were averaged until the signal-to-noise ratio exceeded 1% between 100 and 250 cm^{-1}. The absolute value of the room temperature reflectivity was found using the grating

spectrometer described earlier, and used to normalize the data shown here.

To bring out the weak structure observed, the dual cavity was used. About 80% of the cavity was lined with sample. Fig. 2.9 shows the ratio of intensity transmitted through the sample cavity to that of the polished brass cavity at various temperatures. The structure is obviously much stronger. Ten modes can be identified in the range 40-250 cm^{-1}.

Table 2.1

Beamsplitters, filters, and their effective frequency ranges in cm^{-1}. Black polyethylene was always use attenuate the visible and near-infrared.

$\bar{\nu}_{low}$	$\bar{\nu}_{high}$	Beamsplitter	Filters
40	80	100 G	cooled Y-cut quartz and NaCl
60	200	50 G	cooled Y-cut quartz and LiF
90	250	25 G	room temperature Y-cut quartz
90	350	25 G	pyrolytic boron nitride
120	600	15 G	black polyethylene

Figure 2.1

Resistivity of 1T-TaS_2 vs. temperature normalized to $9X10^{-4}$ ohm-cm at 295 K.

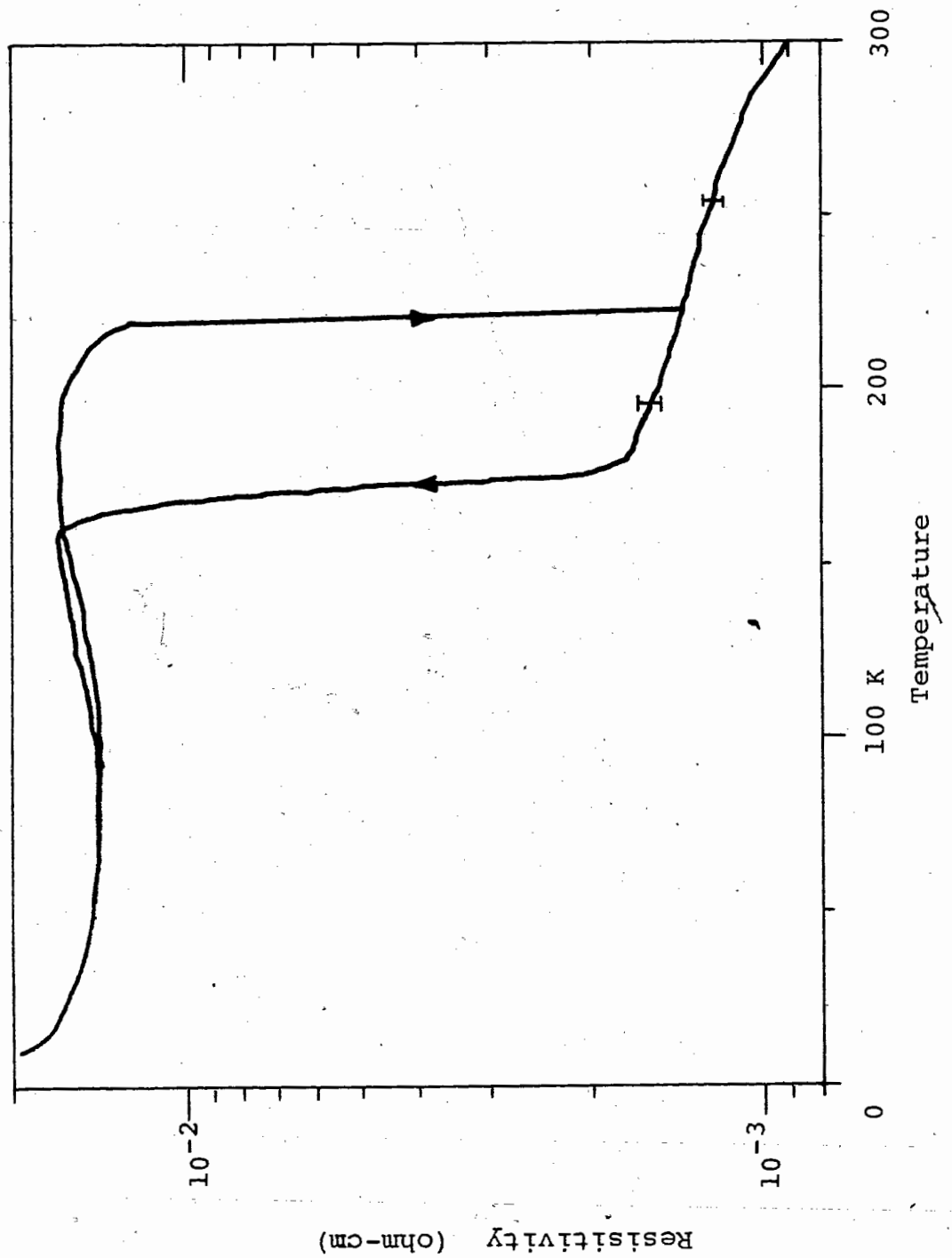

Figure 2.2

Resisitivity of 1T-$TaSe_2$ vs. temperature.

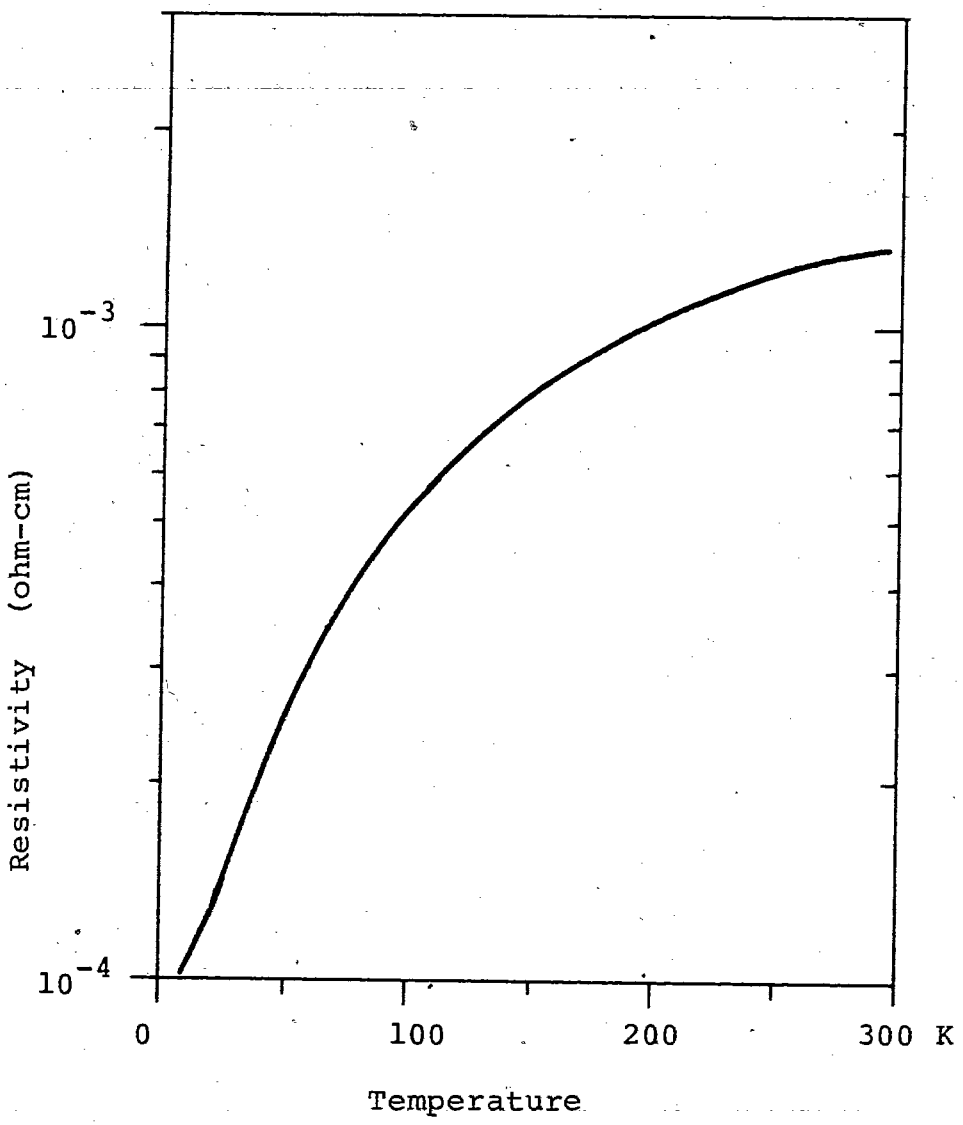

Figure 2.3

Sample insert for reflectivity measurements at 15° incidence at liquid He temperatures.

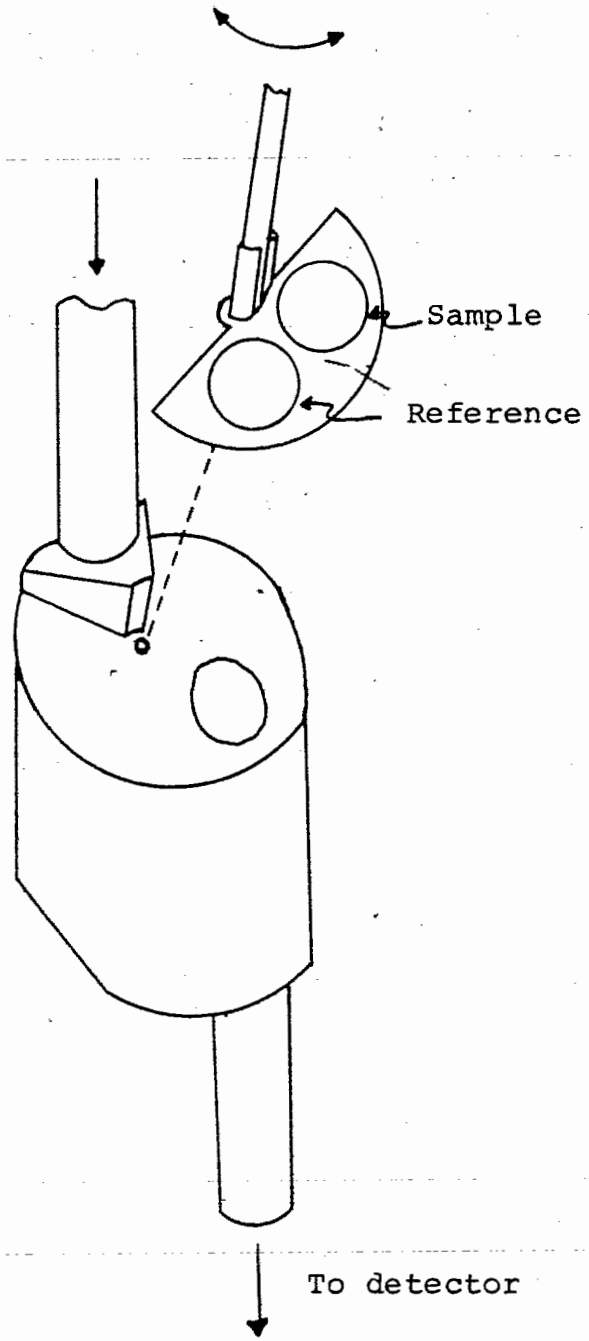

Figure 2.4a) Sample configuration at 15° incidence and T > 80 K.

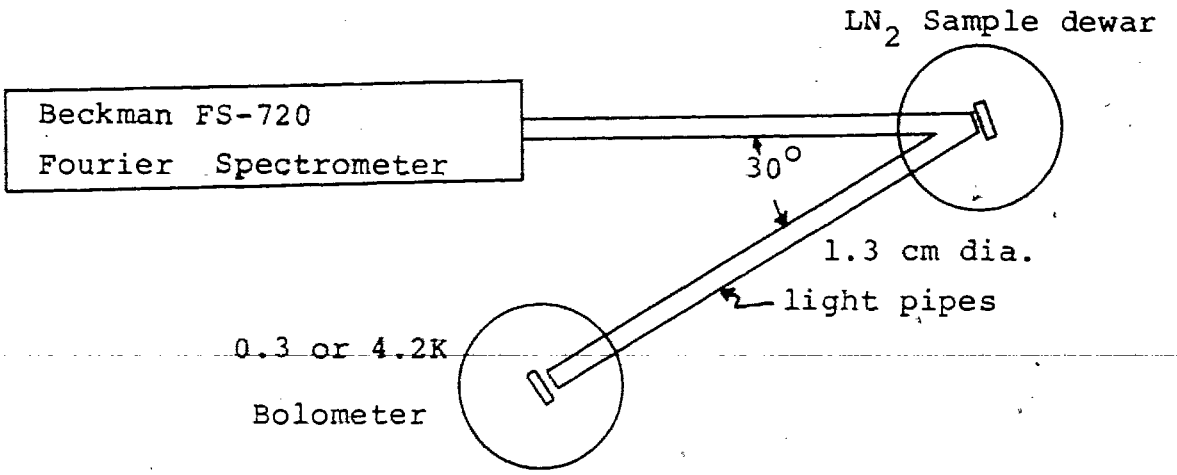

15° incidence

b) Sample configuration for polarization measurements at 45° incidence.

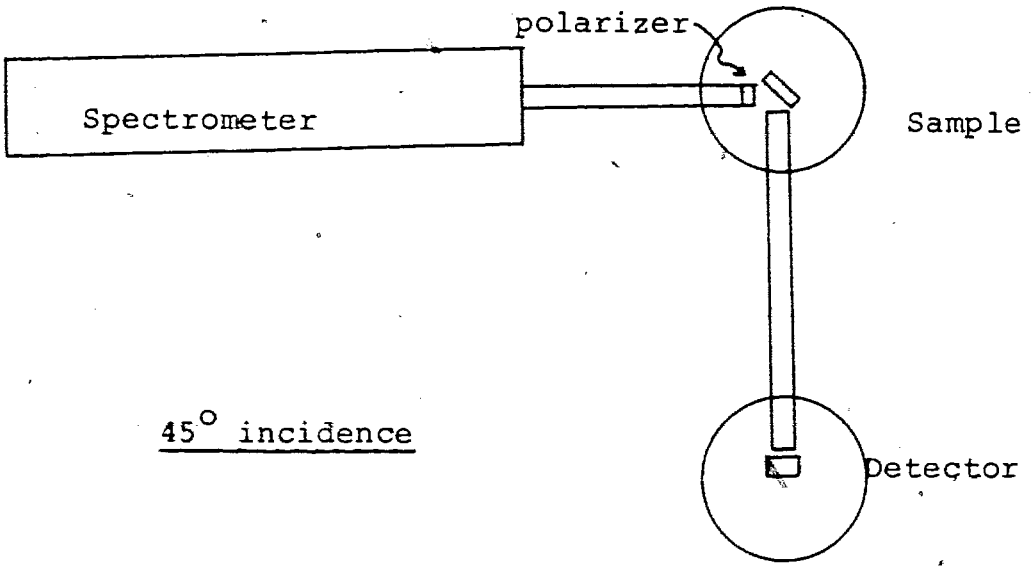

45° incidence

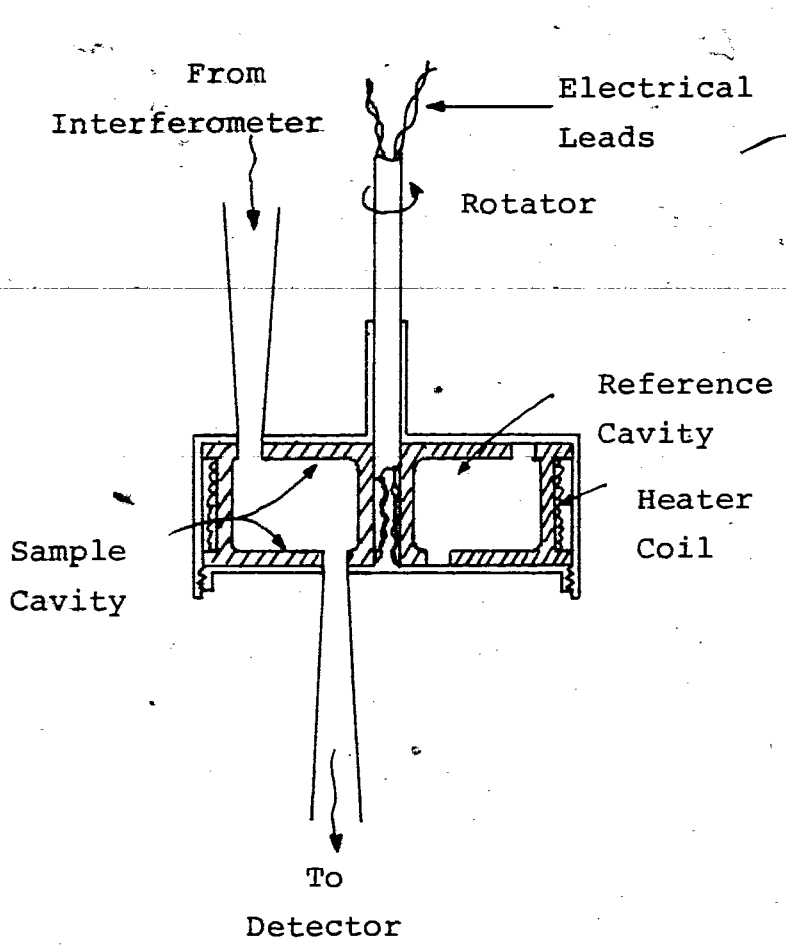

Figure 2.5.

Cross-sectional view of dual cavity.

(After Ward (1976). Full scale).

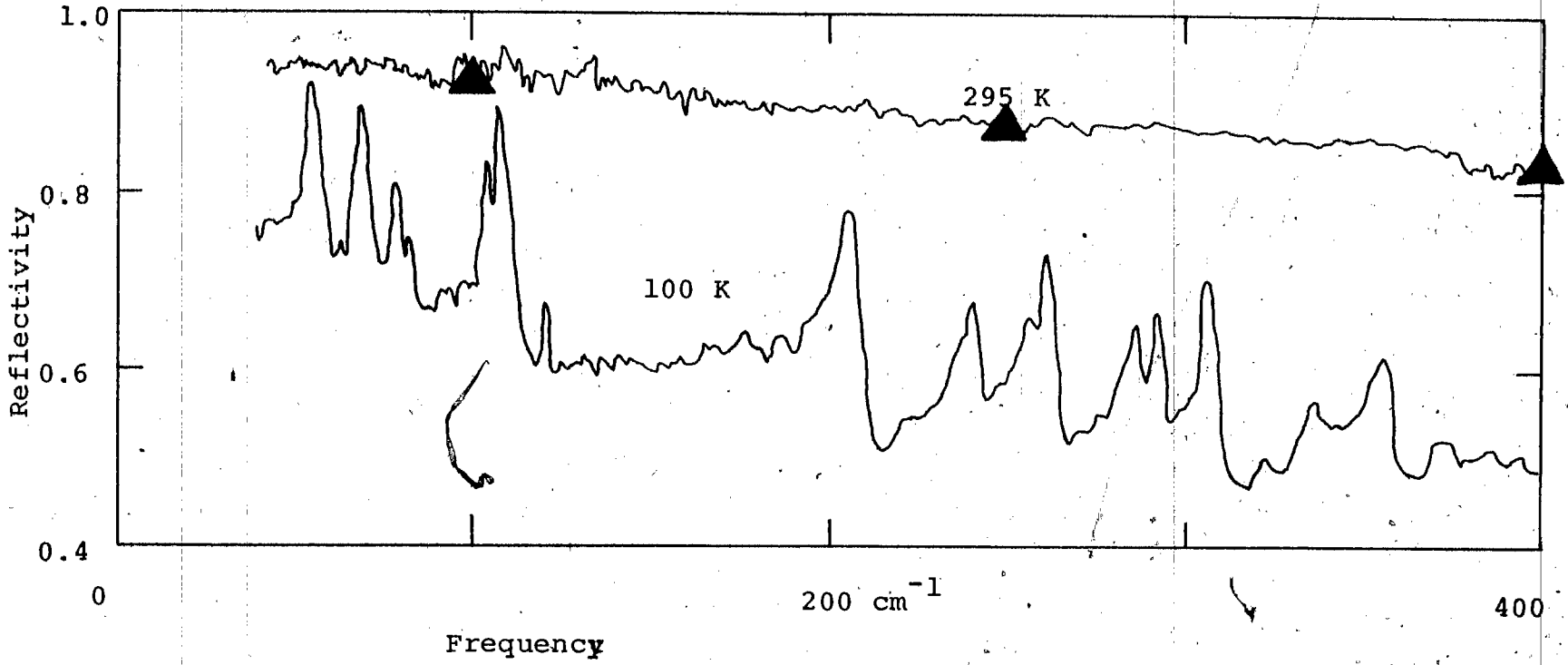

Figure 2.6. Reflectivity of 1T-TaS_2 at 15° incidence in the QCDW phase (295 K) and CCDW phase (100 K) vs. frequency. Resolution is 2 cm^{-1} above and .1 cm^{-1} below 200 cm^{-1}. ▲ are points calculated from the Hagen-Rubens relation.

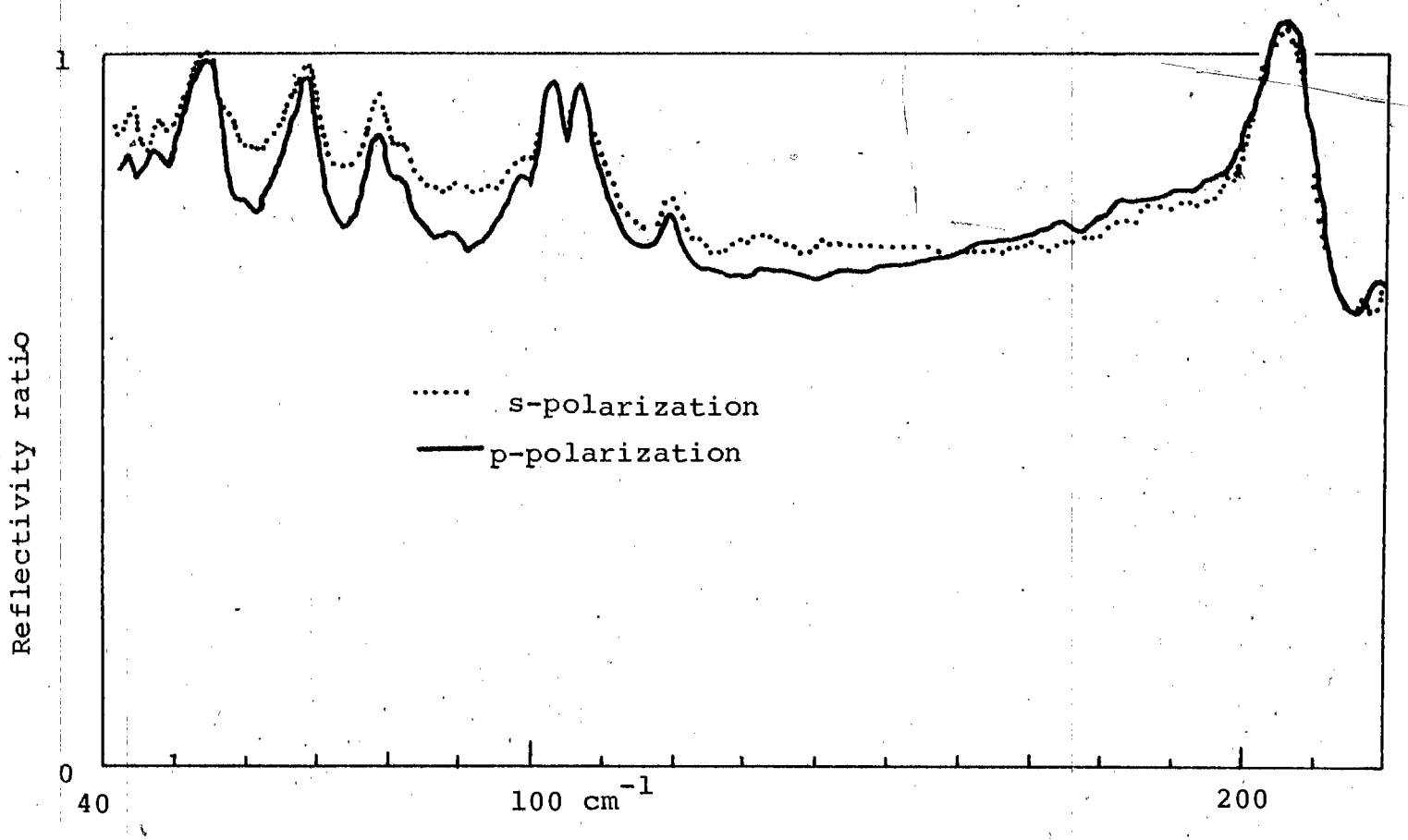

Figure 2.7. Ratio of 100 K 1T-TaS_2 reflectivity to 295 K reflectivity with polarizer in place vs. frequency.

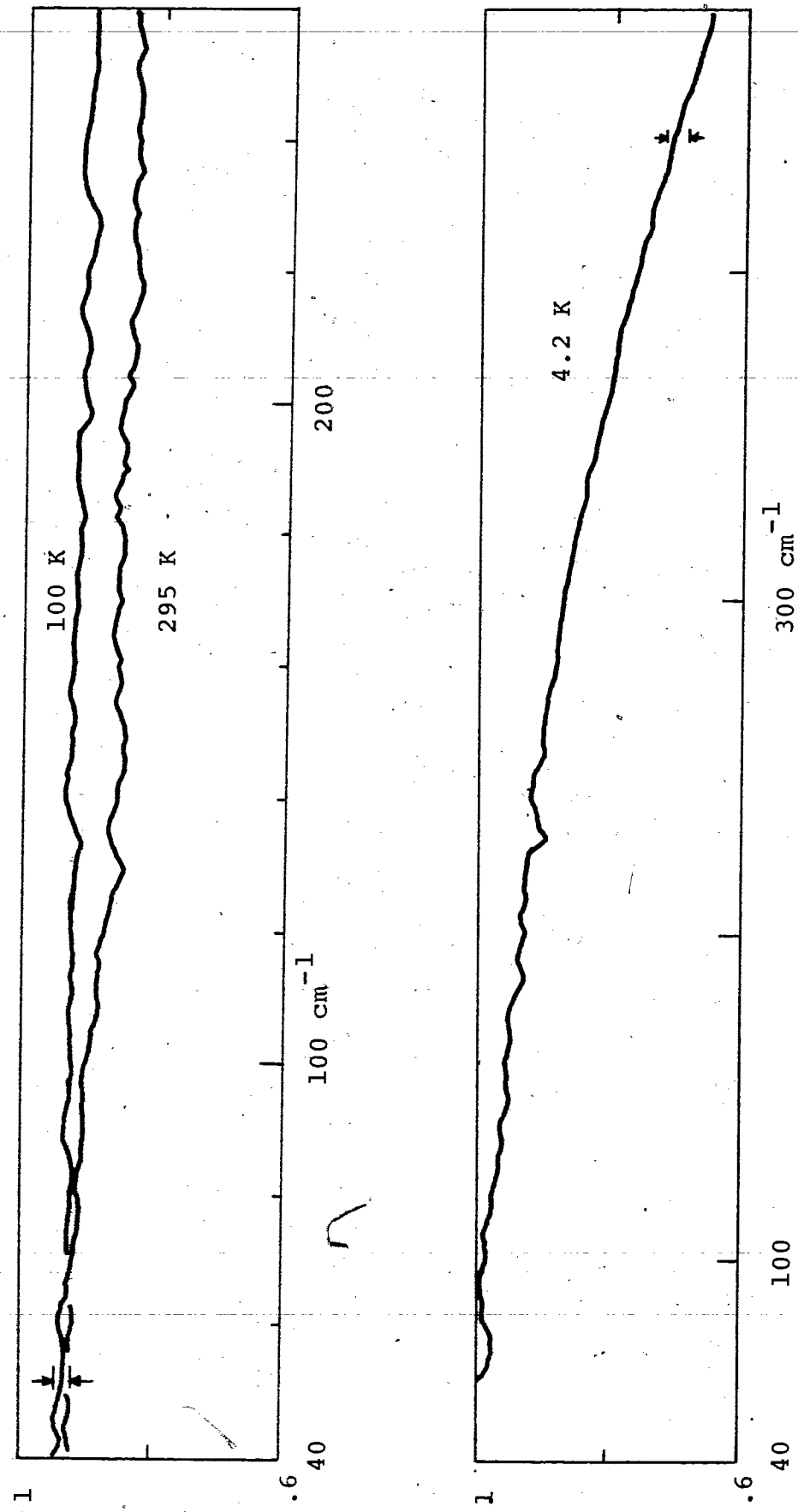

Figure 2.8. Reflectivity of 1T-$TaSe_2$ in theCCDW phase.

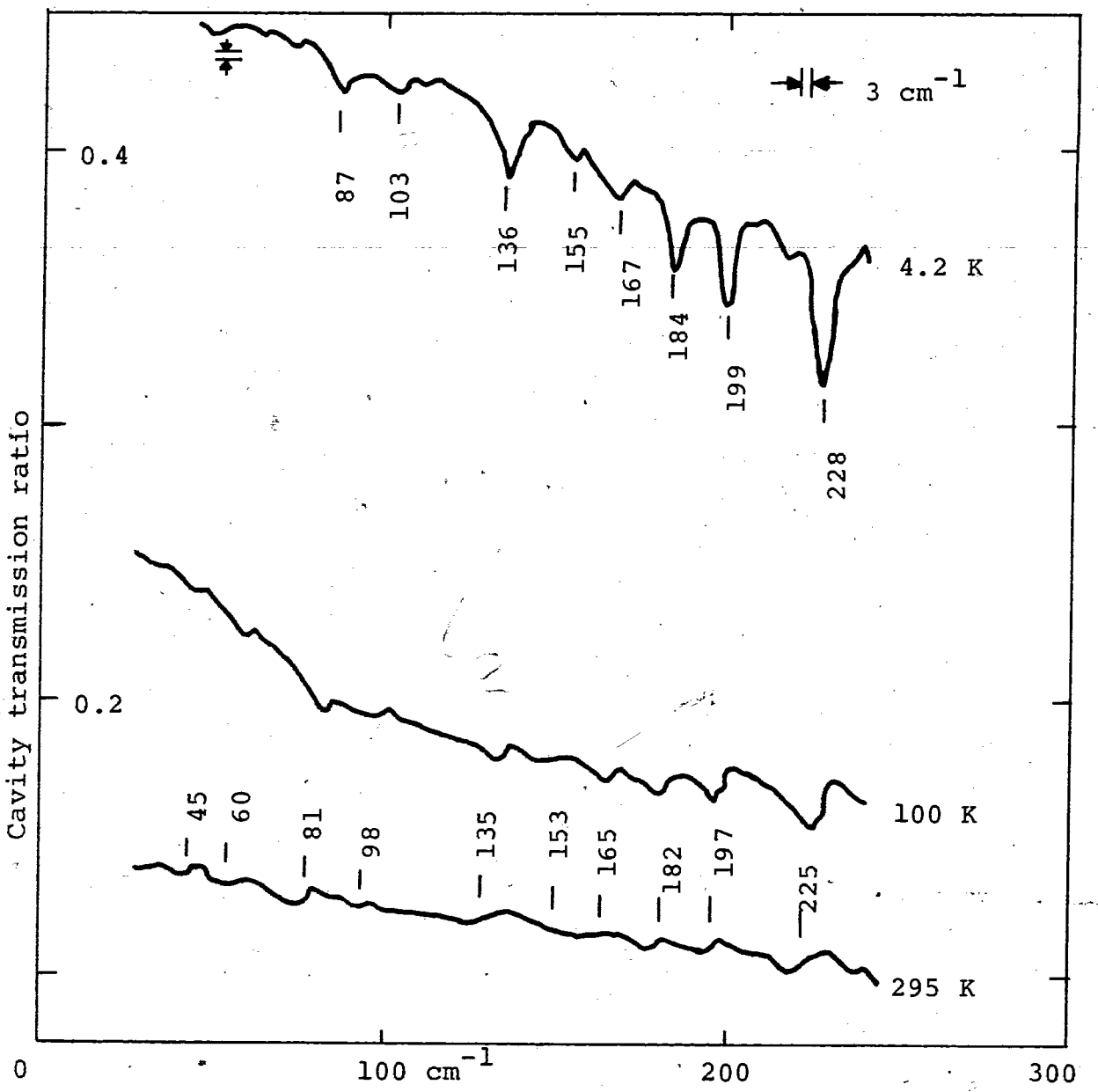

Figure 2.9

Cavity transmission ratio, $I(TaSe_2)/I(brass)$, vs. frequency at various temperatures.

Chapter 3. Determination of optical constants.

The reflectivity data of the preceeding chapter were analyzed in two ways in order to determine the optical constants. If the reflectivity over a wide frequency range is known, a Kramers-Kronig analysis can be performed. An oscillator fit can also be done. These two methods are described in this chapter. At the end, a semi-quantitative fit is made to the multireflection spectra using parameters deduced from the single reflection fits.

A. Kramers-Kronig analysis.

The Kramers-Kronig relations (Hodgson 1970) connect the real and imaginary parts of a function. This function, ε, must have frequency as its argument and relate two quantities obeying causality. For instance: $D=\varepsilon E$. The quantity D can only depend on the values of quantity E in the past.

In terms of the reflectivity at normal incidence, $R=|r^2|$, and phase angle, θ, between the incident and reflected ray ($r_r=r_i e^{i\theta}$), these relations give

$$\theta(\omega)=(1/\pi)\int_0^{\infty} d\omega'(\ln R(\omega')\omega'/(\omega^2-\omega'^2)). \quad (3.1)$$

This equation was evaluated numerically. The singularities

at $\omega=\omega'$ were negotiated by using L'Hôspital's rule. Low frequencies were extrapolated using the oscillator fit described in the next section. This is essentially a Hagen-Rubens extrapolation. High frequencies were obtained from the data of Barker (1975). The optical conductivity calculated from the analysis is shown in Fig. 3.1.

The transverse optical (TO) frequencies of the lattice modes were determined from peaks in the absolute value of the dielectric constant, $|\varepsilon|$. (Chang et al. 1968). They are tabulated in Table 3.1. Longitudinal mode frequencies were estimated from the minima in $|\varepsilon|$. Unless a mode is isolated from neighbors, this is probably not a good estimate. The resolution of the data is 0.5 cm^{-1} at frequencies below 80 cm^{-1}, 1 cm^{-1} until 132 cm^{-1}, and 2 cm^{-1} at higher frequencies.

A similar analysis was not done for 1T-$TaSe_2$ because data were not available at higher frequencies.

B. Oscillator fits.

1. Theory.

Infrared electromagnetic radiation couples to a solid through currents and polarization as described by Maxwell's

equations. Experiments can determine the parameters used in the macroscopic Maxwell's equations, for instance $\varepsilon(\omega)$, where $D=\varepsilon E$. From this the optical constants n and k can be determined from $\sqrt{\varepsilon}=n+ik$. The optical conductivity is obtained from $\sigma(\omega)= \mathrm{Im}(\varepsilon)/4\pi$.

A Lorentz oscillator can be used to describe either phonons or interband electronic transitions. Simple classical and more involved quantum mechanical calculations all lead to an expression of the Lorentz form

$$\varepsilon_i=A_i/(\omega_i^2-\omega^2-i\omega/\tau_i) \qquad (3.2)$$

for the contribution to the dielectric constant from the i-th oscillator. ω_i is the resonance frequency and τ_i is the relaxation time used to describe damping. A_i is a constant that can be related to microscopic models. The separate contributions to the dielectric constant are summed.

Far-infrared photons are almost always too low in energy to excite any interband transitions. Setting $\omega=0$ and summing over all possible transitions,

$$\varepsilon_\infty=1+\sum_i f_i/\omega_i^2. \qquad (3.3)$$

f_i is called the oscillator strength. In the following

discussions ε_∞ will be taken as a constant used to fit experiment.

Intraband electronic transitions can be described by letting $\omega_i=0$. This corresponds to having no restoring force. This contribution to the dielectric constant is called the Drude term.

The total dielectric constant can then be written as the sum of various contributions,

$$\varepsilon(\omega)=\varepsilon_\infty+\sum_i S_i\omega_{oi}^2/(\omega_{oi}^2-\omega^2-i\omega/\tau_i)$$

$$-\sum_i \omega_p^2/(\omega(\omega+2\pi ciG_i)) \qquad (3.4)$$

The first term comes from the electronic polarizability or interband transitions. The second term is a sum of Lorentz oscillators accounting for phonon excitations. A_i has been written as $S_i\omega_{oi}^2$ to simplify the form of other formulae. Note that S_i is dimensionless.

The third term accounts for free carrier intraband electronic transitions (plasmons). A_i has been written as ω_{pi}^2 because in the free electron model when the electronic polarizability is negligible, this would be the frequency of a longitudinal plasma resonance. The relaxation

time has been replaced with $1/\tau_i = 2\pi c G_i$ so that a fit can be made with the damping parameter in units of wavenumbers. Frequency ω is converted to wavenumbers $\bar{\nu}$ by means of $\bar{\nu} = 1/\lambda = \nu/c = \omega/2\pi c$.

The dielectric constant is related to the reflectivity at normal incidence by (Ziman 1969) $R = \left|(\sqrt{\varepsilon} - 1)/(\sqrt{\varepsilon} + 1)\right|^2$. (3.5)

It follows from (3.4) that when $G \gg \bar{\nu}$, only the ratio $\bar{\nu}_p^2/G$ can be determined by a Drude fit and not the two parameters separately. It can also be seen that the value of ε_∞ is not especially critical to the reflectivity in the case where $\bar{\nu}_p^2/G \gg \varepsilon_\infty$. This is the same approximation made in deriving the Hagen-Rubens relation for the reflectivity at normal incidence,

$$1 - R = \sqrt{2\omega/\pi\sigma_o} \qquad (3.6).$$

2. Application.

A least squares fit of Eq., (3.4) to the experimentally determined reflectivity was performed using the CURFIT searching procedure described by Bevington (1969). Lorentz and Drude terms were added until a satisfactory fit was obtained.

3. Results.

1. 1T-TaS_2 at 100 K.

The procedure described above was used to fit the 1T-TaS_2 spectrum of Fig. 2.7. A total of 19 Lorentz oscillators were used, a 60 parameter fit in all. Only the parameters associated with stronger modes are listed in Table 3.2. Mode frequencies agree to within 1 cm^{-1} with those obtained from the Kramers-Kronig analysis listed in Table 3.1. Fig. 3.2 shows the fit achieved. Two sets of the parameters ε_∞, $\bar{\nu}_p$, and G that fit the data equally well are given in Table 3.2.

The optical constants n and k ($\sqrt{\varepsilon}$ =n+ik) calculated from the oscillator fit compare well with those obtained from the Kramers-Krönig analysis described above. At the Lorentz oscillator peaks the calculated reflectivities differed by as much as 25%, but this is not significant in view of the digitizing procedure and sharpness of the peaks. Away from the peaks, n agreed within 2% and k within 10% between the two methods of analysis.

2. 1T-$TaSe_2$

Determining the phonon Lorentz parameters accurately in the presence of a large Drude contribution requires that the background electronic spectrum be fit to high accuracy, better

than 1%. Lucovsky et al. (1976) have done this for the six high frequency modes of 1T-$TaSe_2$ at room temperature. Their fitting parameters are listed in Table 3.3. We were unable to deduce phonon parameters more accurately than this. As a result these values were used in all the fits described here. Only the Drude parameters $\bar{\nu}_p$ and G_i were determined from 1T-$TaSe_2$ spectra.

a. 295 K.

A fit to better than 2% over the range 50-500 cm^{-1} can be made with Drude parameters deduced from the DC conductivity. $\bar{\nu}_p^2 c/(2G)/9x10^{11}=\sigma_o$ mho/cm. For $G < 550$ cm^{-1} and $\bar{\nu}_p < 5000$ cm^{-1}, the fit was not as good, the reflectivity dropping off too fast with increasing frequency. The value of ε_∞ used was not critical to the fit and set at $\varepsilon_\infty = 47$. This is the value reported by Lucovsky et al. (1976). Fig. 3.3 summarizes the results.

b. 100 K.

Here with ε_∞ fixed at 47, a fit with ν_p^2/G at the DC value was higher than experiment by up to 4% (Fit A). If ε_∞ was allowed to vary, a slightly better fit was obtained with lower values of all parameters (Fit B). The results are listed in Fig. 3.4. σ_o deduced from fit B was 1244 mho/cm about a

third of the DC value of 3570.

c. 4.2 K

At this temperature, if all three Drude parameters were allowed to vary, a large value of ε_∞ resulted, around 1000. Furthermore, all the dips in the calculated spectrum vanished, in disagreement with experiment. If ε_∞ were fixed at a reasonable value, around 47, both $\bar{\nu}_p$ and G were much smaller than at higher temperatures. Extending the experiment past the value of $\bar{\nu}_p/\sqrt{\varepsilon_\infty}$ might help to determine them more accurately.

Fig. 3.5 shows a fit with ε_∞ fixed at 29, the same value found to fit the data best at 100 K. The size of the dips at each Lorentz oscillator frequency depend strongly on the value of G. The value of G=117±25 cm^{-1} obtained gave good account of the dips observed. A value of $\bar{\nu}_p$=2911 cm^{-1} was also obtained. σ_o deduced from this fit was only about 20% of the DC value of about 10^4 mho/cm. This is not surprising as the fit is too low at lower frequencies.

Just changing ε_∞ to 47 caused the calculated reflectivity to drop off much too rapidly with frequency. A fit with ε_∞ fixed at 47 gave $\bar{\nu}_p$=3644 and G=137 cm^{-1}. The dips were a little smaller than for the ε_∞ =29 fit.

The dips in the low temperature reflectivity at each phonon mode occur near the TO frequency. The frequencies determined by Lucovsky et al. (1976) at room temperature are about 2 cm^{-1} too low to fit the spectra at 4.2 K. If the phonon TO frequencies are obtained from the minima in the multireflection spectra of Fig. 2.9, the fit is better. To show the approximate agreement with experimental spectra the calculated spectrum tilted slightly to coincide with experiment, as is shown in the inset of Fig. 3.5. This is a crude way of accounting for the non-Drude-like electronic background.

If a second Drude term is introduced, the fit will obviously be better. If ε_∞ is allowed to vary one gets the dotted line fit of Fig. 3.6. σ_o deduced from this is 1.18×10^4 mho/cm in good agreement with the DC value of 0.99×10^4. If ε_∞ is fixed at 47 a similar fit, not shown, is obtained. σ_o here is deduced as 1.32×10^4. Both fits used $\bar{\nu}_{oi}$ from minima in the multireflection spectra. The $\bar{\nu}_o$=228 dip appeared at 226 cm^{-1} in the plot. That is, the dip appears about 2 cm^{-1} lower than the Lorentz frequency.

C. Cavity model.

A model used by Richards and Tinkham (1960) for the transmission through a cavity has application here. They

associated a "Q" with each part of the cavity. Since 1/Q is proportional to the total energy loss per second, one may write the following : $1/Q=1/Q_{walls}+1/Q_{entrance}+1/Q_{exit}$.

The entrance and exit holes have absorptivity of unity, obviously, and their $Q=8\pi V/(A_h \lambda)$, where A_h is the area of the hole and V is the cavity volume. For an isotropic metal, Lamb (1946) has found that, averaged over all angles of incidence, $Q_{walls}=6\pi V/(A \lambda A_w)$, where A is the absorptivity of the walls at normal incidence. A_w is the wall area. A=1-R for thick walls, R being the reflectivity. For 1T-$TaSe_2$ only R at near normal incidence is known. It would have to be multiplied by some unknown factor, set equal to unity here in order to account precisely for the value averaged over all angles of incidence.

The cavity results of Fig. 2.6 are in the form of ratios. If the Hagen-Rubens relation (3.5) is used for the reflectivity of brass, and the oscillator parameters of Figs. 3.3,3.5 and 3.6 are used to calculate the 1T-$TaSe_2$ reflectivity, a theoretical cavity transmission ratio can be obtained. This is plotted in Fig. 3.7.

At the two higher temperatures, the agreement with experiment, Fig. 2.9, is fairly good. However, the calculation for 4.2 K has too much slope on it to agree with experiment. A

reflectivity measurement, not reported earlier, taken at 45° incidence on 1T-$TaSe_2$ at 4.2 K showed less of a drop with increasing frequency than the near-normal incidence measurements. The too rapid slope of the 4.2 K calculation may be associated with not having integrated the reflectivity over all angles of incidence.

The phonon resonances in the cavity calculation show good agreement with experiment. The Lorentz parameters used to fit the phonon contribution to the reflectivity were those of Lucovsky et al.(1976). They are listed in Table 3.3. Comparing these with the 1T-TaS_2 parameters listed in Table 3.2, one finds good agreement of the parameter S for the six high frequency modes.

One might then expect that similar values of the parameter S would also be appropriate for the low frequency modes of both crystals. If this is assumed, and the additional phonon modes are included in the calculation of the cavity transmission ratio, the reflectivity of these modes is too large to agree with experiment. Values of S about 20% of the 1T-TaS_2 values are more realistic. This estimate is the best that can be done since these low frequency modes were too weak to be seen in a single reflection with the apparatus used here.

Table 3.1

Transverse optical frequencies determined from a Kramers-Kronig analysis of the 1T-TaS_2 reflectivity in the CCDW phase. The frequencies of strong modes are underlined. Longitudinal optical frequencies are in parentheses.

Low frequencies (cm^{-1})

54, (58), 58.5(61), 63.5(64.5), 66.5(67), 68.5(73), 75.5(76), 78(81), 82(83.5), 88(89), 94(95), 97(99), 104(106), 107(114), 115(118), 120(123), 125(126), 131(132)

High frequencies (cm^{-1})

182(190), 204(212), 240(244), 256(258), 260(266), 286(288), 292(296), 306(312), 322(326), 354(362), 370(378), 386(390) 394(398)

Table 3.2. Fitting parameters for 1T-TaS_2 at 100 K

ε_∞=40 $\bar{\nu}_p$=2.8X10^{4}cm^{-1} G=1.9X10^{5}cm^{-1}

or

48 1536 cm^{-1} 524 cm^{-1}

$\bar{\nu}_o$(cm^{-1})	S	τ(10^{12}sec)
54	23	3.1
68	9.6	2.8
78	4.7	1.1
104	5.7	1.9
107	2.1	5.4
204	2.4	1.5
241	0.66	1.8
256	0.52	1.0
261	0.89	1.4
286	0.41	1.6
292	0.51	1.4
306	0.76	1.3
355	0.57	0.8

Table 3.3

Lucovsky's (1976) Lorentz parameters for 1T-$TaSe_2$ at 295 K

$\varepsilon_\infty = 47$

$\bar{\nu}_o$	S	$\tau (10^{12}$ sec)
135.1	2.4	0.82
152.8	0.6	1.40
165.4	0.7	1.52
182.3	0.7	1.47
196.7	0.6	1.08
224.9	0.5	1.40

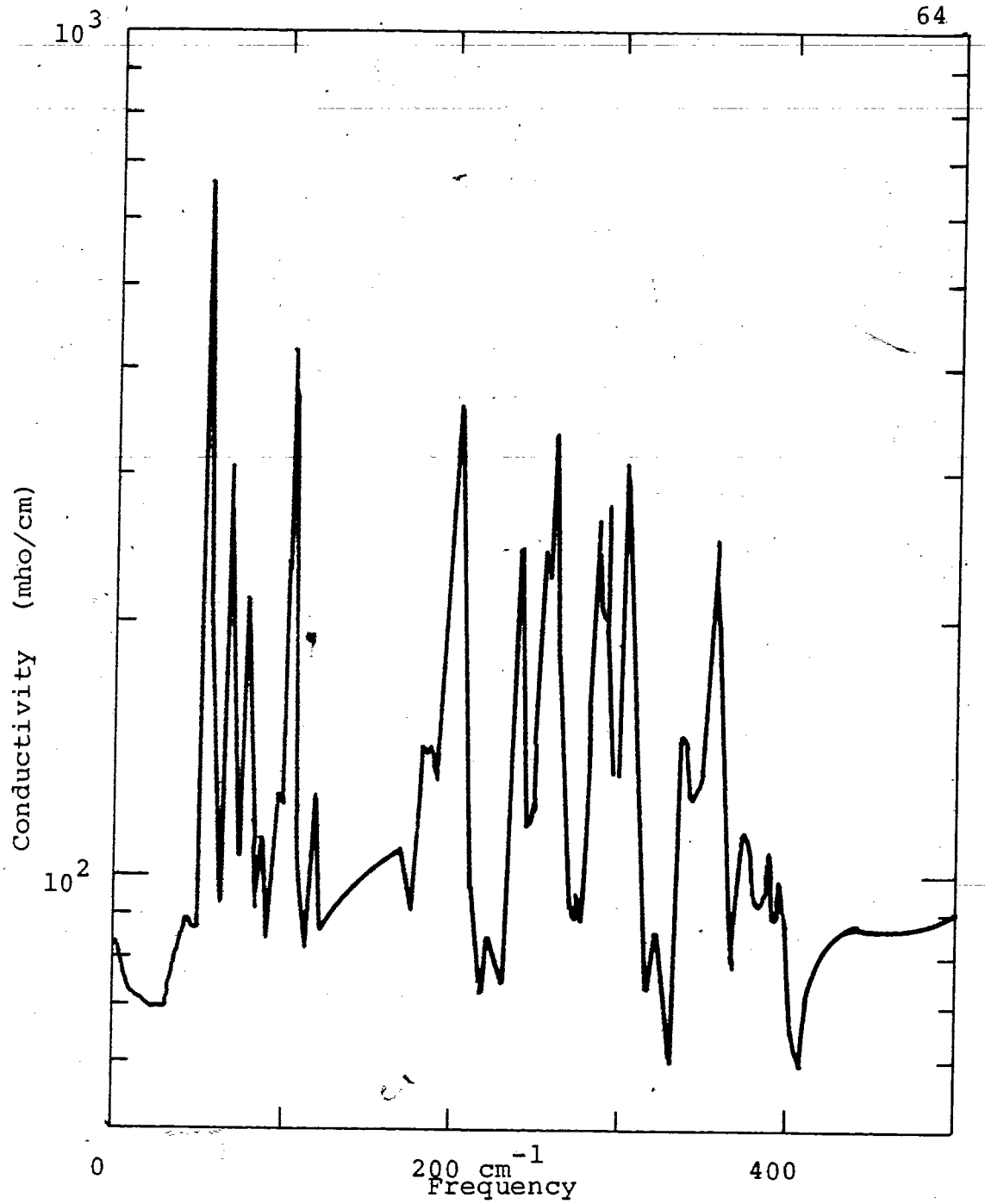

Figure 3.1

Optical conductivity of 1T-TaS_2 at 100 K calculated from a Kramers-Kronig analysis.

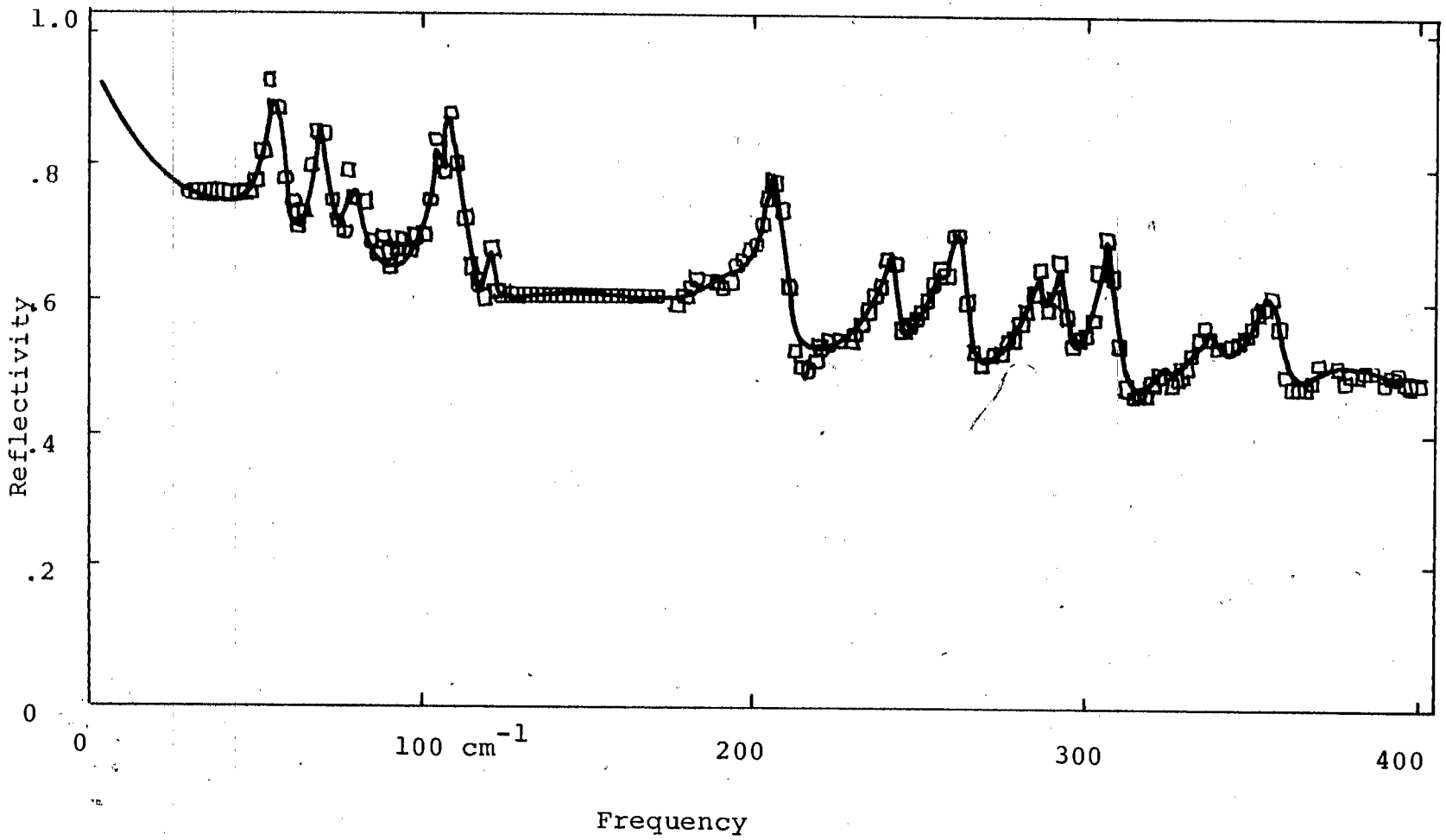

Figure 3.2. Oscillator fit to 1T-TaS_2 reflectivity at 100 K. □ expt.

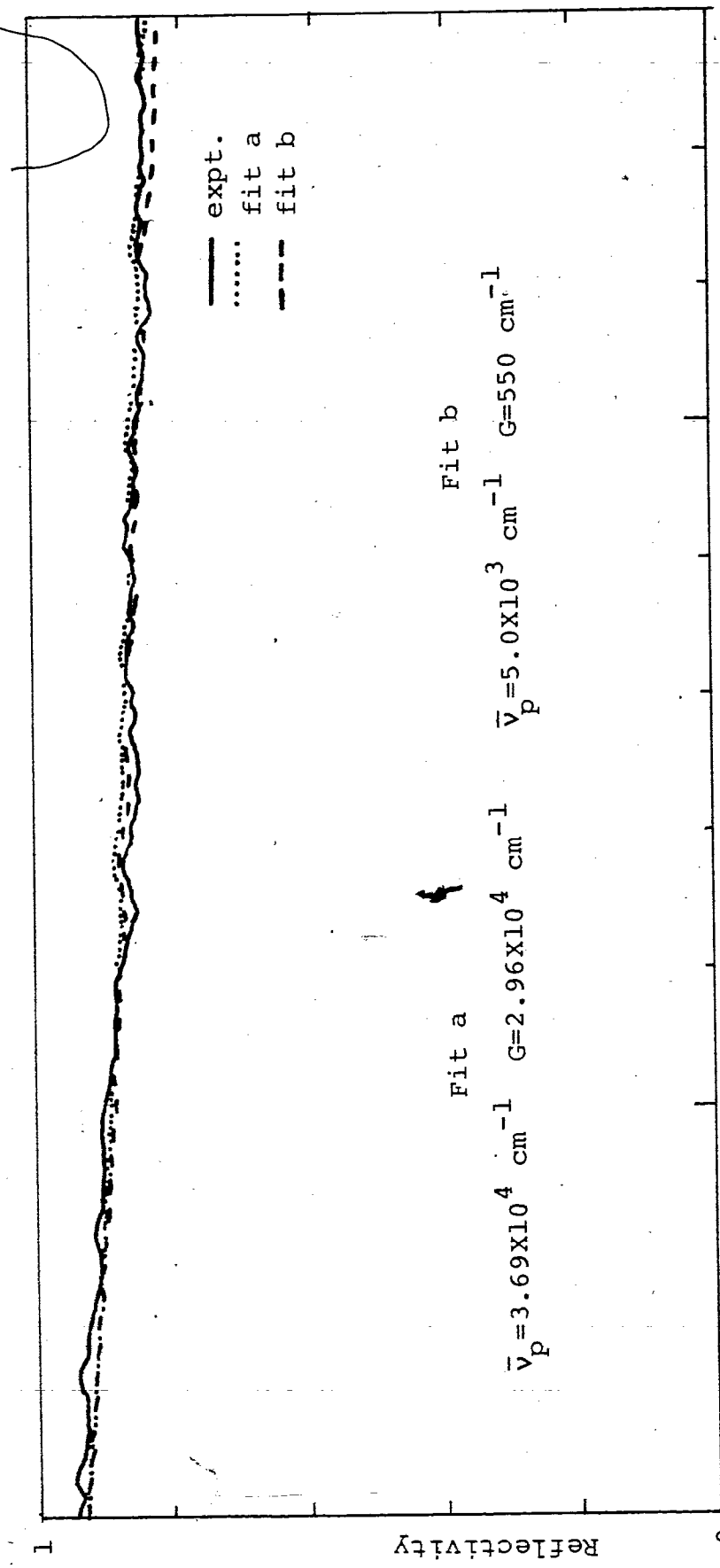

Figure 3.3. Oscillator fit to 1T-$TaSe_2$ reflectivity at 295 K. ϵ_∞=47.

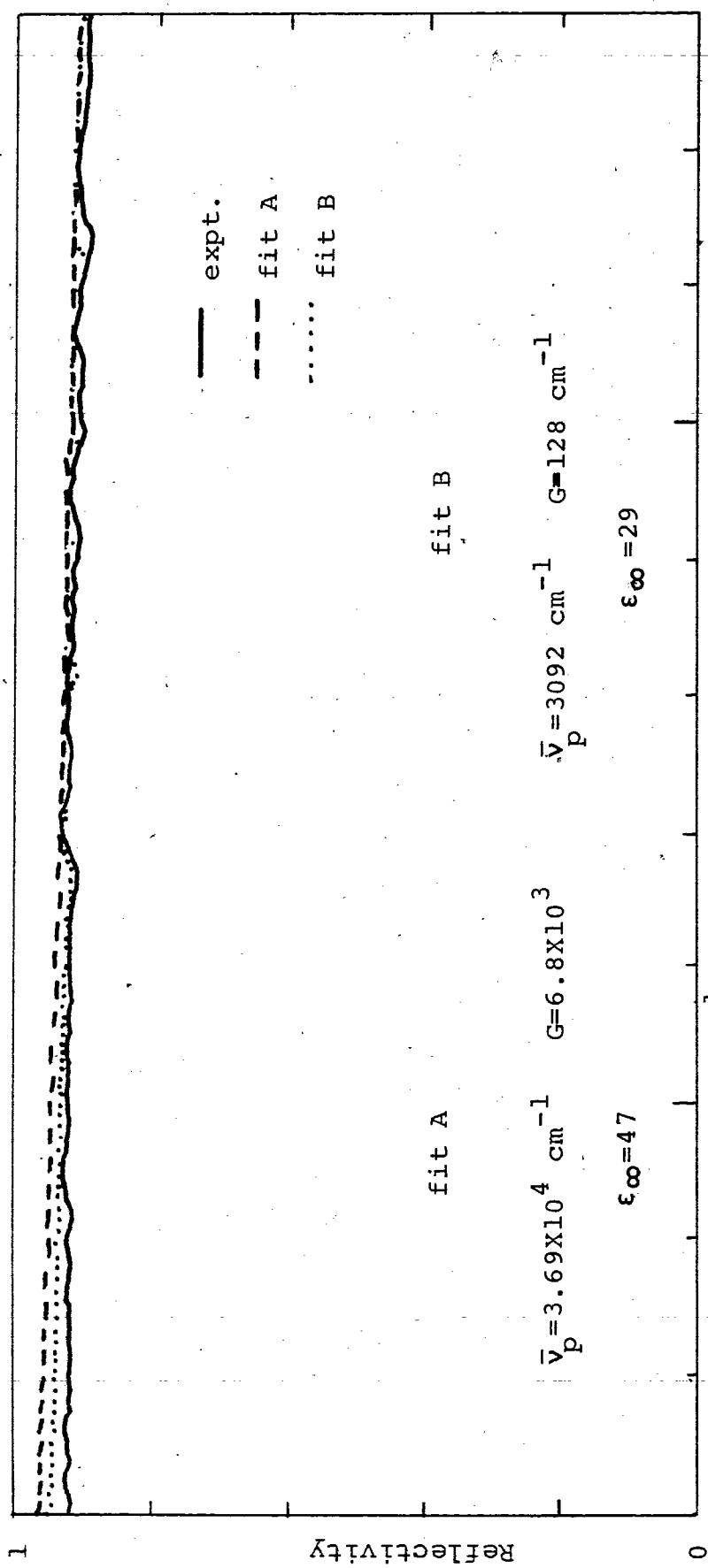

Figure 3.4. Oscillator fits to 1T-$TaSe_2$ reflectivity at 100 K.

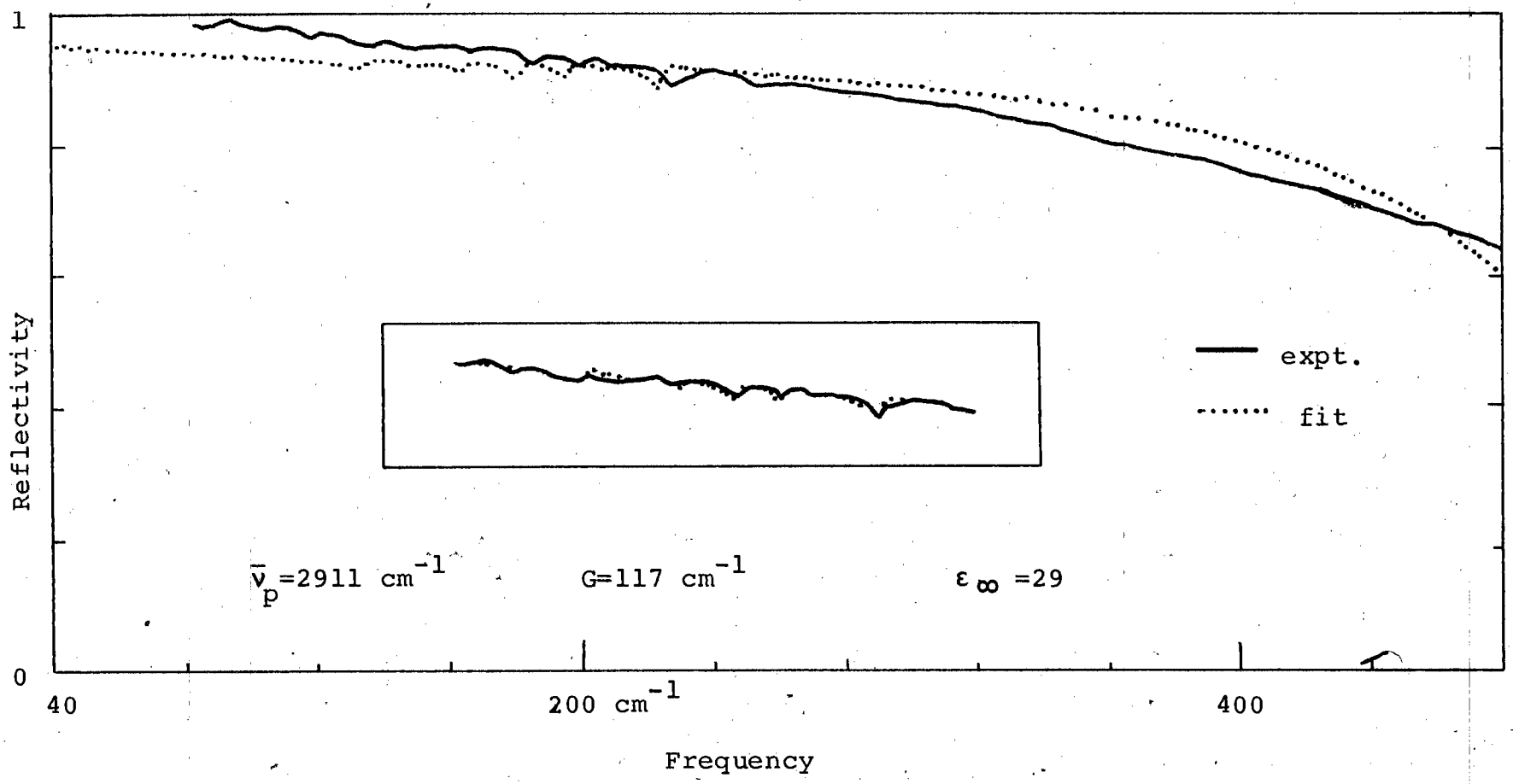

Figure 3.5. Single oscillator fit to 1T-$TaSe_2$ reflectivity at 4.2 K. Inset described in text.

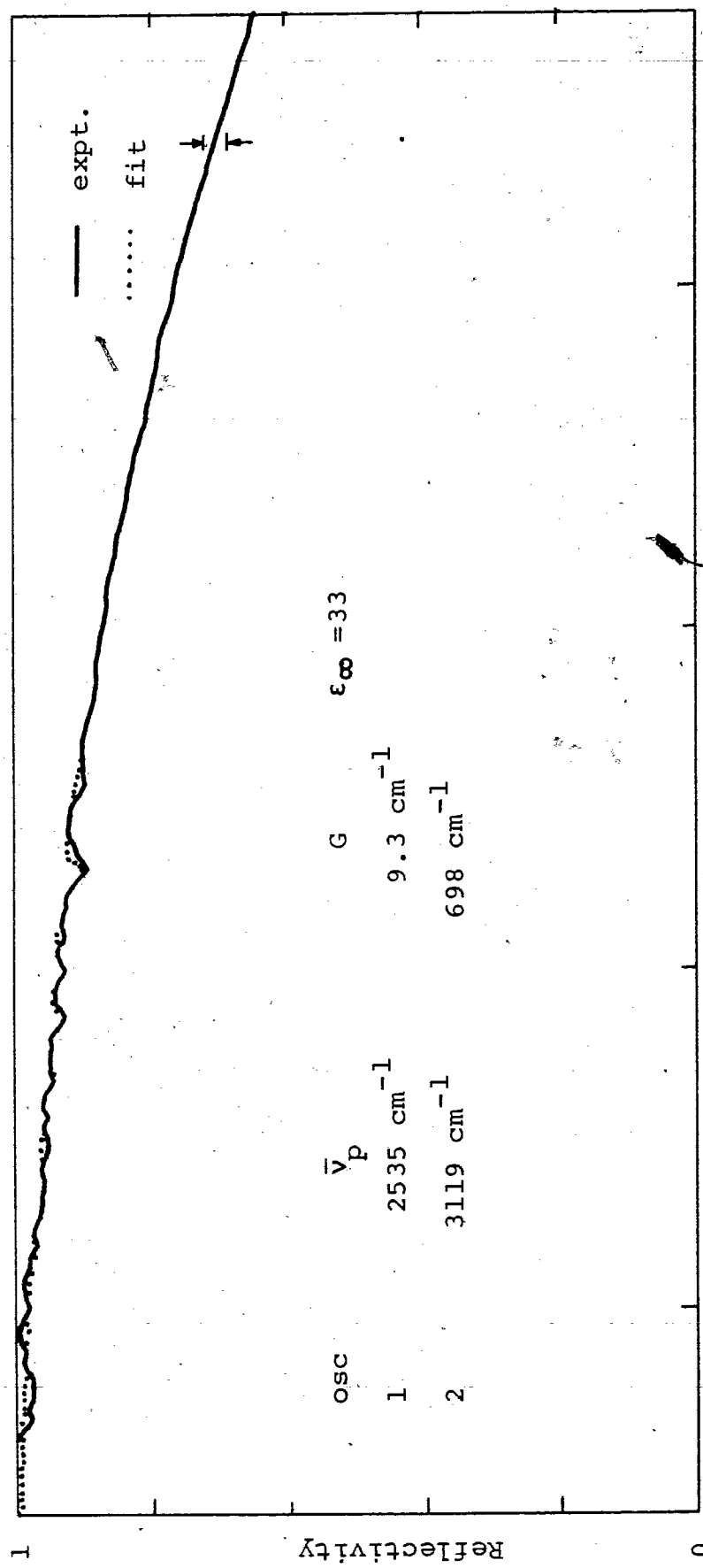

Figure 3.6. Oscillator fit to 1T-$TaSe_2$ reflectivity at 4.2 K using two Drude terms.

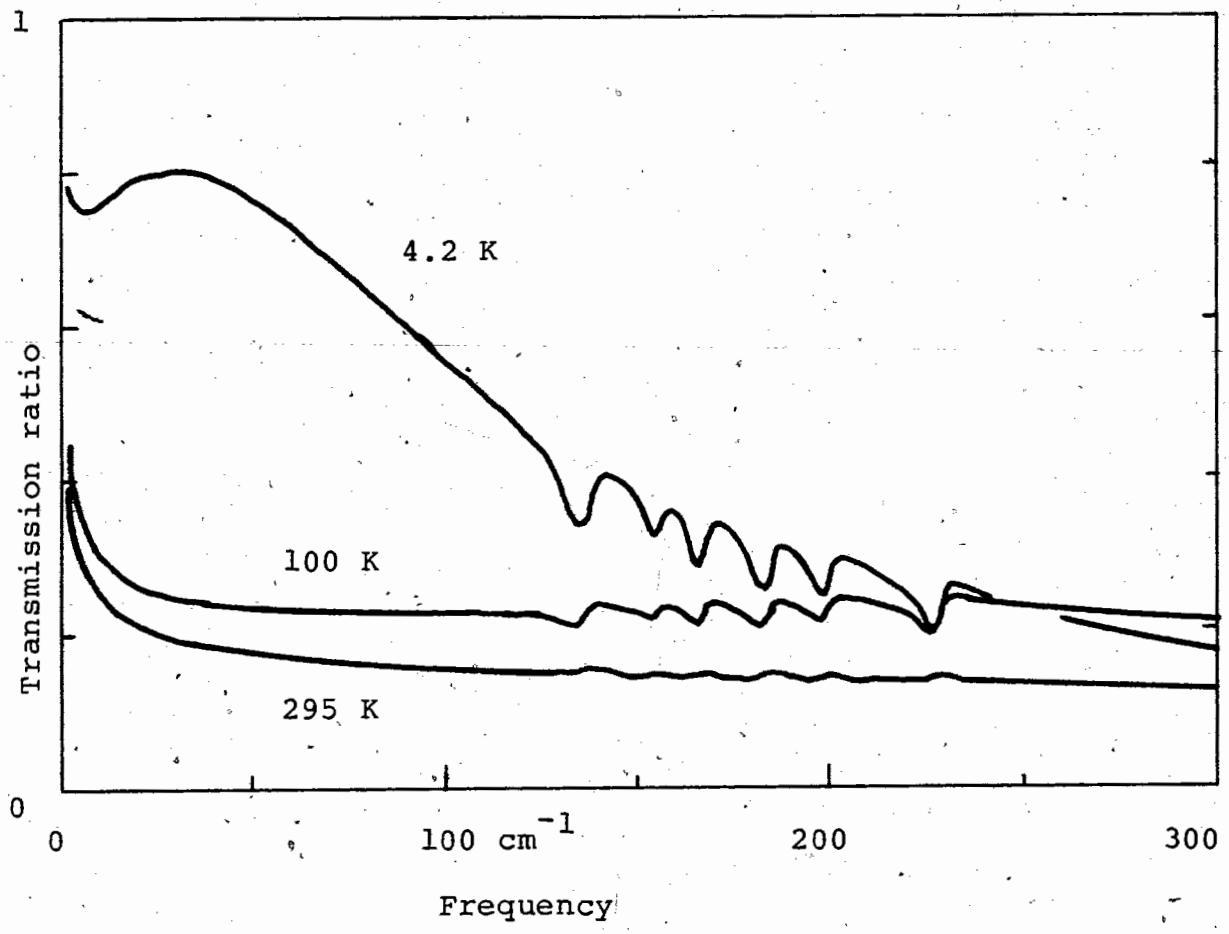

Figure 3.7

Theoretical cavity transmission ratio for 1T-$TaSe_2$.

Chapter 4. Discussion of phonon results.

The oscillator fits described in chapter 3 determined three parameters for each phonon mode; the frequency, $\bar{\nu}_{oi}$; the relaxation time, τ_i; and the strength, S_i. A discussion of the damping is outside the scope of this thesis. Part A of this chapter will be an attempt to explain the phonon frequencies observed in both 1T-TaS_2 and 1T-$TaSe_2$. Part B will discuss the parameters S_i in terms of effective charges. The temperature dependence of the spectra is associated with the electronic contribution of the plasmon term and will be discussed in Chapter V.

A. Phonon frequencies.

1. Linear chain model.

The linear chain model is the simplest lattice dynamical model. It is discussed in most elementary solid state textbooks (Kittel 1966). Expressions for the frequencies in the long wavelength limit from more realistic models frequently reduce to those of the linear chain model with suitable identification of force constants and mode masses.

Wieting (1973) has used the linear chain model to study the lattice dynamics of 2H-MoS_2. It is easily adapted to fit the

1T-CdI_2 structure. The expression $\omega_o^2=k_{eff}/\bar{m}$ has a value of the effective force constant, k_{eff}, and mode mass, $\bar{m}$, for each type of long wavelength mode (Fig. 1.3). For the E_g Raman mode, $\bar{m}=m(2I)$ (mass of two iodine atoms). For the infrared E_u mode, $\bar{m}=m(Cd)m(2I)/(m(Cd)+m(2I))$ (Appendix I).

The effective force constants for compounds related to 1T-TaS_2 and 1T-$TaSe_2$ will be discussed first. The E_u force constants for the compounds whose optical phonon frequencies are listed in Table 1.2 follow certain trends. k_{eff} is always greater for the sulphides than for the selenides of a particular cation. k_{eff} increases down a column of the periodic table. For the group VIB compounds, k_{eff} is more nearly constant than for the group IVB compounds. Less data are available from group VB compounds due to their more metallic nature. The above variation down a column is less than 27% for the group IVB compounds and less than 6% for the group VIB compounds.

Moving across a row, where mode masses are nearly equal, it is easily seen that k_{eff} increases significantly. The lower values of the group IVB force constants are undoubtedly due partly to local field effects. These are greater in more ionic compounds. (Burstein 1967,1971). Evidently the group VB compounds are somewhat intermediate to groups IVB and VIB. The presence of CDW distortions complicates the comparison.

The linear chain model can also make some prediction on how the phonon modes in the 2H compounds should compare with the 1T compounds. Verble (1973) used it to show that the near degeneracy between the 2H E_u and $E_{2g}{}^1$ mode frequencies was due to weak interaction between the two layers in the unit cell. The 2H-TaS_2 and 2H-$TaSe_2$ E_u frequencies should be near to the observed Raman frequencies of 285 and 207 cm^{-1} respectively. It can be argued that the 1T and 2H force constants are approximately equal, at least near the zone center in the nearest-neighbor approximation. Duffey (1978) has modified Bromley's (1971) central force model, used for only one trigonally coordinated layer in the 2H system, for the octahedrally coordinated 1T case. The E_u mode frequencies predicted were identical. Assuming the same nearest neighbor force constants, the 1T and 2H structures should have the same E_u mode frequency, that predicted above.

Infrared-active phonons have been observed in the present experiments near to these frequencies in the CCDW phase of both crystals: 286 cm^{-1} for 1T-TaS_2 and 197 cm^{-1} for 1T-$TaSe_2$. (Table 4.2). This is not to be taken as conclusive evidence that these observed modes derive from the E_u modes of the undistorted lattices. The CDW affects the binding between atoms to an unknown extent. The effect of electronic screening on the long range interactions is also not known. Further work

is needed to resolve this problem. A determination of the phonon dispersion curves by inelastic neutron scattering in the ICDW phase of both compounds would be most helpful.

2. Central force models.

Bromley (1971) used a simple central force Born-von Karman model to describe the lattice dynamics of 2H-MoS_2. The model is two dimensional in the sense that k_z=0. Three parameters must be determined from optical experiments or calculated from microscopic models. Duffey (1978) modified Bromley's model to describe the 1T-TaS_2 case. He estimated one parameter and determined the other two from his experimentally determined Raman frequencies: an E_g mode at 240 and an A_{1g} mode at 385 cm^{-1}.

Duffey used these frequencies because they appeared in the QCDW as well as CCDW phase. It is by no means clear that these correspond to the E_g and A_{1g} modes of the undistorted lattice. In undistorted 2H-TaS_2, the E_g mode occurs at 203 cm^{-1} while the A_{1g} mode occurs at 399 cm^{-1} (Table 1.2). As discussed earlier, these modes should be similar in both polytypes of the same compound. The A_{1g} modes are at similar frequencies, but the E modes differ substantially.

Table 4.1 contains the frequencies calculated by Duffey at

the k=0 Γ-point and also at the points $\vec{Q}_1$ and $\vec{Q}_2$. $\vec{Q}_1$ and $\vec{Q}_2$ are reciprocal superlattice wavevectors that appear in the Brillouin zone of the undistorted lattice in the CCDW phase. This is shown in Fig. 4.1. Thirteen points are labelled along the direction of the $\vec{Q}_1$ wavevector which connects the origin to point "2". This point is one of the inner six points of a "star" surrounding each lattice point of the Brillouin zone of the undistorted lattice. $\vec{Q}_2$ is the wavevector of the point "3", at the outer points of the star. The frequencies calculated at the six inner points are equal, as are those for the outer points. Hence, only the frequencies calculated at $\vec{Q}_1$ and $\vec{Q}_2$ are given in Table 4.1.

In Fig. 4.1, the superlattice points are origins of the superlattice Brillouin zone. Stated another way, the frequencies at k≠0 branches of the undistorted lattice become folded in to k=0 points of the new, smaller Brillouin zone of the CCDW phase superlattice. The parts of the phonon branches folded in to k=0 are those at the CCDW distortion wavevector.

The CCDW phase unit cell has thirteen times as many atoms as that of the undistorted 1T-CdI_2 structure. Each of the nine phonon branches of the simpler structure splits into thirteen branches under the influence of the CCDW distortion. This is just an extension of the idea that the optic branch of a diatomic linear chain can be thought of as arising from the

folding in of the acoustic branch of a monatomic linear chain. Gapping could remove the degeneracy so that the twelve points of the star in Fig. 4.1 could have twelve different frequencies instead of the two calculated in this model. Many near degeneracies could still remain.

3. Comparison of calculated and observed frequencies.

Duffey's (1978) model is just a first attempt at understanding the very complex lattice dynamics of a large unit cell with CDW distortions. No neutron data are available for comparison. Detailed agreement with the observed Raman and infrared spectra is not obtained with this model.

This model predicts a gap between modes arising from the acoustic and optic branches of the undistorted material. Between 137 and 215 cm^{-1}, no modes are predicted. This corresponds fairly well with what is observed (Table 3.1). Holy (1977) attributed a weak Raman-active mode at 183 cm^{-1} to a two phonon process. The weak mode in the infrared spectrum at 182 cm^{-1} may also be due to such a process. This mode was somewhat stronger in the spectra reported by Karecki and Clayman (1976) on a different batch of 1T-TaS_2 crystals. Little temperature dependence of this, or indeed, any mode was observed from 4.2 to 180 K.

The upper limit of the calculated frequencies also agrees well with what was observed. The upper limit of the calculation appears to be fixed by the choice of frequency for the A_{1g} mode. The calculation also has a lower limit close to that observed. A detailed comparison of theory and experiment is unwarranted in view of the simplicity of the model.

5. Comparison of infrared-active modes in CCDW 1T-TaS_2 and 1T-$TaSe_2$.

Since the form of the CCDW phase superlattice for these two materials is the same, they should have the same number of phonon modes but at different frequencies due to the heavier Se atom. Since S and Se are from the same column of the periodic table, the force constants are expected to be similar.

The presence of more free carriers has been seen to screen out the phonons more in the 1T-$TaSe_2$ case. Thus a comparison with only the strongest modes of 1T-TaS_2 seems appropriate. This has been done in Table 4.2. The 1T-TaS_2 frequencies are from oscillator fits. The four lowest 1T-$TaSe_2$ frequencies are estimates from the experimental reflectivity. The remaining six frequencies were obtained by Lucovsky et al. (1976) and agree with those observed here.

The ratios of mode freqencies with the correspondence listed are given in Table 4.2. For the six high frequency modes, the ratios are remarkably close to the square root of the inverse ratio of anion masses, 1.57. For the four low frequency modes, the ratios are close to one.

The simple linear chain model of Section 1 can explain the results as follows. At the zone edge, $\bar{m}=m(2S)$ for optic modes, but $\bar{m}=m(Ta)$ for acoustic modes. At the zone center, $\bar{m}=m(2S)m(Ta)/(m(2S)+m(Ta))$ for optic modes, and $\bar{m}=m(Ta)+m(2S)$ for acoustic modes.

Thus, if equal force constants are assumed, the ratio of mode frequencies of corresponding modes in 1T-TaS_2 and 1T-$TaSe_2$ should go as the inverse square root of their mode mass ratio. For optic modes, it should vary between 1.34 at the zone center to 1.57 at the zone edge. For acoustic modes, it should vary from 1.18 to 1.00 in going from the zone center to the edge.

This implies that the four low frequency modes derive from acoustic branches of the undistorted crystal. The six high frequency modes appear to derive from optic modes. This is in agreement with the lattice dynamical calculations discussed earlier (Table 4.1).

The nearly exact agreement of the ratios of the six high frequency modes with the inverse square root of the anion masses is not to be taken as conclusive evidence that the mode mass is that of the anions. As mentioned earlier in Section 1, the effective force constants for the E_u modes of the related compounds listed in Table 1.2 are consistently higher for the sulphides than for the selenides. This together with the zone center mode mass given just above could equally well explain the data. It does not change the interpretation of their origin from optic modes of the undistorted material.

6. Comparison of experimental infrared and Raman spectra.

a. 1T-TaS_2.

When a site of inversion symmetry is present in a crystal, the infrared and Raman modes can only be accidentally degenerate. Examination of the experimental data shown in Table 4.3 might at first glance indicate that, since the frequencies observed in the Raman and infrared spectra are not identical, a site of inversion is present. Of the two possible space groups with a triclinic unit cell, C_i^1 and C_1, the former would then be the most likely.

However, it is quite possible that all the modes were not observed in any of the experiments. Many observed modes were at

the limit of detectability. Even if the modes seem to be degenerate, they would have to be assigned to the irreducible representations of the point group of small displacements from equilibrium before a statement could be made about their degeneracy. With 39 atoms in a unit cell and uncertainty about the space group, this problem is presently intractable. It can thus only be speculated, based mainly on the absence of any mode in the infrared spectra near the 228 cm^{-1} mode in the Raman spectra, that the space group of the superlattice of 1T-TaS_2 in the CCDW phase is C_i^1.

b. 1T-$TaSe_2$.

Duffey (1978) has also seen mode multiplicity in Raman spectra of 1T-$TaSe_2$ in the CCDW phase. At 90 K, where the spectrum is more distinct than at higher temperatures, he found the modes listed in Table 4.4. The infrared-active modes which are listed in Table 4.2 are also given. The same reservations about possible degeneracy discussed for 1T-TaS_2 apply here even more strongly due to the greater difficulty in observing these modes.

The strong modes at 135 and 153 cm^{-1} observed in the infrared spectrum have no counterparts in the Raman spectrum. Based on the discussion of Section 5, the mode at 135 cm^{-1} corresponds to the mode at 204 cm^{-1} seen in the spectrum of

1T-TaS_2 in the CCDW phase, strongly in the infrared but only weakly in the Raman spectrum (Table 4.3). This mode could easily have been missed in Duffey's work. The penetration of laser light into the sample is less for more metallic 1T-$TaSe_2$ than for 1T-TaS_2, so that the scattered light would be weaker.

The modes in the Raman spectrum of 1T-$TaSe_2$ extend to higher frequencies than the modes observed in the infrared. Since the highest frequency infrared-active modes were weak in the 1T-TaS_2 spectrum, it is likely that the corresponding modes in 1T-$TaSe_2$ were too weak to be observed with the apparatus used here. In conclusion, even less can be deduced from a comparison of infrared and Raman spectra in the CCDW phase of 1T-$TaSe_2$ than could be determined from the 1T-TaS_2 due to the difficulties in studying a more metallic crystal.

7. Comparison of 1T-$TiSe_2$ and 1T-$TaSe_2$ infrared spectra in the CCDW phase.

Below 200 K, a CCDW state appears in 1T-$TiSe_2$. The superlattice unit cell is double the size of that of the undistorted state in all directions. As a result, eight times as many phonon branches are present. Holy et al. (1977) and Liang et al. (1979) have seen mode multiplicity in the infrared spectra of these materials. Their results are given in Table 4.5 along with the frequencies seen here for 1T-$TaSe_2$.

The agreement in frequencies of these two compounds whose cations differ in mass by almost a factor of four is remarkable. Their superlattices in the CCDW state are different. This means that modes are not folded in from the same places of the dispersion curves of the undistorted material.

At least part of the agreement is due to stiffer force constants in the Group VB compounds (Section 1). A more detailed explanation is not possible at present. The wavevector dependence of the dielectric constant which screens the interaction between atoms is not known in detail. It is not known if 1T-$TaSe_2$ exhibits a Kohn anomaly as does 1T-TaS_2 (Ziebeck 1977). At least in the normal state, at room temperature, 1T-$TiSe_2$ does not show evidence of a Kohn anomaly (Stirling et al. 1976).

The origin of most of the modes seen in the simpler 1T-$TiSe_2$ case have been assigned to branches of the phonon dispersion curves in the undistorted state. (Holy et al. 1977, Jaswal 1979). This is not feasible for 1T-$TaSe_2$ where even the space group is unknown. Further work is needed if Table 4.5 is to be fully understood.

B. Effective charges.

An effective charge on each atom can, in principle, be calculated from parameters determined from an oscillator fit to the reflectivity. The macroscopic Born transverse effective charge, e_T^*, is given by

$$e_T^* = c\,\bar{\nu}_{oi}(\pi \bar{m} S_i/n)^{1/2}. \qquad (4.1)$$

(Burstein 1967, 1971). $\bar{\nu}_{oi}$ is the TO frequency in wavenumbers. n is the oscillator density. $\bar{m}$ is the mode mass which is determined by reducing the problem to the form of a diatomic oscillator. The problem with its application here is that the mode masses for the infrared-active modes observed in the CCDW state are not known. As an approximation, the value for the CdI_2 structure may be used as shown in Appendix I:

$$\bar{m} = m(2I)m(Cd)/(m(2I)+m(Cd)).$$

A value of 2.3e for the 204 cm^{-1} 1T-TaS_2 mode and 2.2e for the 135 cm^{-1} 1T-$TaSe_2$ mode are obtained making this guess at the mode mass. Lucovsky et al. (1976) determined the values of the 1T-$TaSe_2$ parameters (Table 3.3). This is the charge on the Ta atom assuming the local field acting on the molecules is the macroscopic field and that the polarizations of the ions and electrons simply add together (Burstein 1967, 1971).

Lucovsky et al. (1976) determined that e_T^* was about 1.6e for 1T-TaS_2 in the QCDW phase from a fit to a mode at 210 cm^{-1}. However they used a mode mass half that used here. This would seem to be in error, as Appendix I makes clear. With double the mode mass, their effective charge for this mode in the QCDW phase agrees with the 204 cm^{-1} mode in the CCDW phase calculated here.

From the work of others, an effective charge can be calculated for the E_u modes of the compounds 1T-HfS_2 and 1T-$HfSe_2$ (Lucovsky et al. 1973) and 2H-MoS_2 (Wieting and Verble 1971). For HfS_2, e_T^*=5.5e. For $HfSe_2$, e_T^*=6.1e. For MoS_2, e_T^*=1.2e.

The value of the effective charge ~2e for the group VB compounds compares with ~6e for the group IVB compounds and e for the group VIB compound. This can be compared with the charge of 4e on an isolated cation. The above is consistent with gradually increasing ionicity in going from group IVB to group VIB.

In the Szigeti polarizable ion model (Burstein 1967), which is most successful with ionic compounds, the effective charge at the ion is given by $e_s=3/(\varepsilon_\infty+2)e_T^*$. That is, the transverse macroscopic effective charge is enhanced due to the presence of a local field at the ion greater than the

macroscopic field. This could partially explain why the effective charge on the Hf compounds is greater than the formal valence of 4e.

In real compounds, one cannot simply add the electronic and ionic polarizations. The shell model allows for the change in electronic polarizability due to ionic motion. It can explain the reduction of effective charge in the ionic case as well as the presence of charge in covalent materials where there is no static charge (Donovan and Angress 1971). A detailed attempt at explaining the effective charge is outside the scope of this thesis.

An attempt to find an effective charge for the low frequency modes in 1T-TaS_2 and 1T-$TaSe_2$ can be made. Earlier, in Chapter 3, section C, it was shown that the parameters S_i for 1T-$TaSe_2$ were about 20% of those for 1T-TaS_2, listed in Table 3.2. Table 4.2 shows that the frequencies of the four strong low frequency modes in both crystals are comparable, implying that their effective masses are nearly equal. In the linear chain model (Kittel 1966), this occur near the zone boundary where $\bar{m}$=m(Ta). This is most likely an underestimate of the mode mass.

This leads to effective charges of 3.7, 3.0, 2.4 and 4.3e for the modes in 1T-TaS_2 at 54, 67, 78 and about 106 cm^{-1}

(combining the 104 and 107 cm^{-1} modes) respectively. The corresponding effective charges in 1T-$TaSe_2$ are about half this. This is a semi-quantitative way of saying that the acoustically-derived infrared-active phonon modes in the CCDW phase of 1T-TaS_2 are appreciably stronger than their counterparts in 1T-$TaSe_2$.

Table 4.1

Phonon frequencies calculated by Duffey (1980) at three points in the Brillouin zone of an undistorted 1T-TaS_2 crystal. Frequencies are in cm^{-1}.

	Γ	$\vec{Q}_1$	$\vec{Q}_2$
$\bar{\nu}_1(TA_1)$	0	65	95
$\bar{\nu}_2(TA_2)$	0	65	95
$\bar{\nu}_3(LA)$	0	104	137
$\bar{\nu}_4(O_1)E_g$	240	260	259
$\bar{\nu}_5(O_2)E_g$	240	267	265
$\bar{\nu}_6(O_3)E_u$	243	222	215
$\bar{\nu}_7(O_4)E_u$	243	230	224
$\bar{\nu}_8(O_5)A_{2u}$	298	307	325
$\bar{\nu}_9(O_6)A_{1g}$	385	377	363

Table 4.2

Dominant phonon frequencies in cm^{-1} in both 1T-TaS_2 and 1T-$TaSe_2$ in the CCDW phases along with the ratio of sulphide to selenide frequencies.

1T-TaS_2	1T-$TaSe_2$	ratio
54	45	1.20
68	60	1.13
78	81	0.96
104	98	1.06
107		1.09
205	135	1.52
241	153	1.58
256	165	1.55
261		1.58
286	182	1.57
292		1.60
306	197	1.55
355	225	1.58

Table 4.3. Summary of experimental optical phonon mode frequencies in the CCDW phase of 1T-TaS_2. Strong IR modes are underlined.

IR (100 K)	Raman (130 K) Holy (1977)	Raman (90 K) Duffey (1978)
54,59,64	62 E_g	56,62
		68,72
67,69,76,78,82	72 E_g, 78 A_{1g}	80
88	89	89
94		
97,104,107,115 120	98 E_g, 112 A_{1g}	100,106,115,121
125,131	126 A_{1g}, 132	129,134
	152(2 phonon)	
182	183(2 phonon)	
204	204(2 phonon)	
	228 A_{1g}	228
240	243 E_g	243
256,260	256 E_g,265 E_g	248,258,265
286,292	277,282,283 A_{1g}	278,282,293
306	297 E_g,306 A_{1g}	298
		308
322	321 A_{1g}	323
336	330 E_g	331,338
355		
370	365 A_{1g},366	364
386,394	386 A_{1g},393	387

Table 4.4. Comparison of IR and Raman (Duffey 1978) mode frequencies in the CCDW phase of 1T-$TaSe_2$.

IR	Raman
45	
	53
60	60
	64
	71
81	80
	85
98	97
	101
	109
135	
153	
165	166
	179
182	
	185
	188
197	
	211
225	223(?)
	239
	249
	270

Table 4.5. Comparison of IR phonon mode frequencies in cm^{-1} in the CCDW phases of 1T-$TaSe_2$ and 1T-$TiSe_2$.

1T-$TaSe_2$	1T-$TiSe_2$ (18 K) Liang et al. (1979)	1T-$TiSe_2$ (20 K) Holy et al. (1977)
45		42
		52
60		64
81		76
98		90
	118	118
135	140	137
153	151	152
165		162
	172	175
182		178
197	197	198
225	213	

Figure 4.1

Basal plane of reciprocal superlattice of CCDW phase. Hexagon is boundary of normal Brillouin zone.

○ Reciprocal point of normal lattice

• Reciprocal point of superlattice

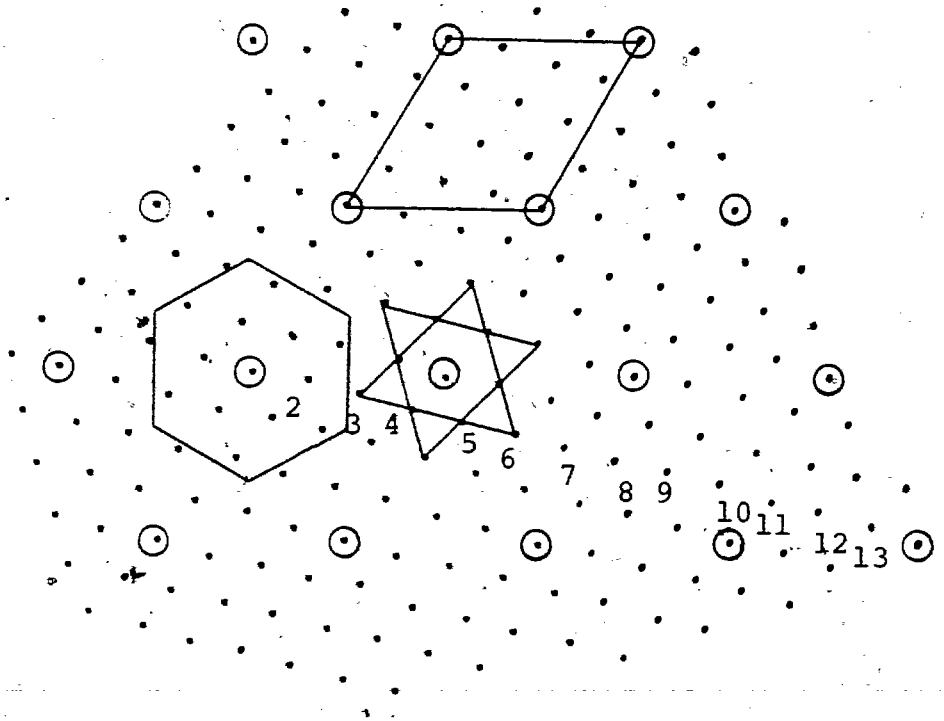

Chapter 5. Discussion of plasmons.

Optical conductivity can be explained in terms of the band theory of solids combined with classical transport theory. (Ashcroft and Mermin 1976. Hodgson 1970). The theory is restricted to photon energies less than the band gap. Interband transitions are thus not described.

If the relaxation time approximation is used to describe scattering, the following expression is obtained for the optical conductivity.

$$\overleftrightarrow{\sigma}^{n}(\omega)=e^2/4\pi^3\int d\vec{k}\left[\frac{\vec{v}_n(\vec{k})\ \vec{v}_n(\vec{k})(-df/dE)}{(1-i\omega\tau_n(\vec{k}))}\right]\tau_n(\vec{k}) \qquad (5.1)$$

n is the band index. The total conductivity is obtained by summing over all bands. $\vec{v}=1/\hbar\ \mathrm{grad}_{\vec{k}}E$ is the electron velocity. f is the Fermi-Dirac distribution function. τ_n is the relaxation time, assumed to vary with k.

If τ is assumed to depend on $\vec{k}$ only through $E(\vec{k})$, the sharp peak of (-df/dE) at the Fermi surface enables τ to be factored out of (5.1) to a good approximation.

$$\overleftrightarrow{\sigma}^{n}(\omega)=\frac{e^2\ \tau(E_f)}{(1-i\omega\tau_n(E_f))}\int d\vec{k}/4\pi^3\ \vec{v}_n(\vec{k})\ \vec{v}_n(\vec{k})(-df/dE) \qquad (5.2)$$

Since f depends on k only through E(k), an integration by parts of (5.2) yields

$$(\overleftrightarrow{\sigma}^{n}(\omega))_{ij}=e^2\tau_n/(1-i\omega\tau_n)\int(dk/4\pi^3)(M^{-1})_{ij} \quad (5.3).$$
$$\equiv e^2(\overleftrightarrow{N/m^*})_{ij}\ \tau_n/(1-i\omega\tau_n)$$

$(\overleftrightarrow{M^{-1}})_{ij}=1/\hbar^2 d^2E/dk_i dk_j$ is the inverse effective mass tensor.

For the free electron model, it is easily seen from (5.3) that $\sigma(\omega)=e^2\tau N/m_e/(1-i\omega\tau)=\sigma_o/(1-i\omega\tau)$, a familiar result, where m_e is the mass of a free electron.

In terms of the contribution to the dielectric constant,

$$\varepsilon f=4\pi i\sigma/\omega=-\omega_p^2/(\omega(\omega-i/\tau)) \qquad (5.4)$$

where $\omega_p^2=4\pi Ne^2/m^*$.

(5.4) is in the form of the last terms of (3.4), used to fit the reflectivity data. The summation of terms like (5.4) comes either from a relaxation time differing over different portions of the Fermi surface or a number of different bands at the Fermi level. The interpretation of ω_p^2 is in terms of N/m^*, the effective carrier density divided by an effective

mass as defined in (5.3).

A fit using terms like (5.4) can not determine N and m^* separately. Other transport measurements, such as the Hall effect or susceptibility, must be performed in order to do this. When $\omega >> 1/\tau$, measurement of the optical conductivity can determine N/m^* separately which can not be done from measurements of the DC conductivity which depends only on their ratio. This will be seen to be the case for 1T-$TaSe_2$ at 4.2 K.

A. 1T-TaS_2

The spectra in the ICDW and QCDW states were adequately explained by the Hagen-Rubens relation (3.6). Evidently the necessary criteria of high conductivity and low frequency range were met. In the CCDW phase at 100 K, since the conductivity is lower than in the two higher temperature phases, a single Drude term was used in fitting the electronic contribution to the CCDW spectrum.

In the oscillator fit to the 1T-TaS_2 reflectivity at 100 K (Fig.3.2 and Table 3.2), values of $\bar{\nu}_p \geq 1500$ cm^{-1} were found to be satisfactory. Lower values caused the reflectivity to drop off too rapidly with increasing frequency. For $\bar{\nu}_p$ much higher than far-infrared frequencies (e.g. $\bar{\nu}_p = 4X10^4$

cm^{-1} in the free electron model), the optical conductivity extrapolated to 67 mho/cm at zero frequency in excellent agreement with the measured value of 70±7 mho/cm. The fit with $\bar{\nu}_p$=1536 cm^{-1} extrapolated to 75 mho/cm, again in excellent agreement. Using this minimum value of $\bar{\nu}_p$, a value of $n \geq 2.6X10^{19}$ cm^{-3} for the single carrier density can be calculated from (5.4), assuming a free electron mass.

These values of carrier concentration may be compared with those obtained from the recent Hall effect measurements of Inada et al.(1979), Uchida et al.(1979), and Tanuma et al. (1979). Above the CCDW transition temperature (ca. 200 K), the carriers were found to be predominantly n-type, while below it, they were predominantly p-type. Assuming a single band model, which obviously fails as R_H is changing signs, the number of carriers may be calculated from $n=-1/R_He$ (MKS).

This gave around $n=10^{22}cm^{-3}$ n-type carriers at 360 K in the ICDW phase, around $n=5X10^{21}cm^{-3}$ n-type carriers at 295 K in the QCDW phase, and around $p=5X10^{18}cm^{-3}$ p-type carriers at 100 K in the CCDW phase for the data of Inada et al. (1979) and Tanuma et al. (1979).

The Hall coefficient was reported only for the CCDW phase by Uchida et al. (1979). Their measured values of R_H were considerably less than those of the other workers. Their data

gives $p=3X10^{19}$, considerably larger than that of the other workers.

At 295 K and 360 K, the values of n calculated from the Hall effect measurements were consistent with those deduced from the optical fits. Together with the measured DC conductivity, they would imply (through $\bar{\nu}_p^2/G=(2/c)\,\sigma_o$) the validity of the Hagen-Rubens relation (3.6). ($\bar{\nu} \ll G$, $\varepsilon \cong i\,\bar{\nu}_p^2/(\bar{\nu}\,G)$).

At 100 K, the values of p deduced from Uchida et al.'s (1979) Hall effect measurements agrees with that calculated from the lower limit of $\bar{\nu}_p$ used in the oscillator fit. The other group's Hall effect measurements give a value about a sixth of this. It is difficult to determine the cause of this discrepancy between the two groups.

The above discussion should have made clear why it is impossible to calculate an effective mass from the combined optical and Hall effect measurements as it is possible to do in principle. The changes in the Fermi surface with temperature are shown dramatically in the Hall effect measurements. The situation is very complex indeed.

The present experiments extend to lower frequencies the infrared reflectivity measurements of 1T-TaS_2 taken by Barker et al. (1975a) in the range 300-40000 cm^{-1}. They found that

the spectra were not of simple Drude form ($Re(\sigma) = \sigma_o/(1+(\omega\tau)^2)$). No sharp gap structure was observed upon cooling into the CCDW phase. As this was done, the conductivity was gradually reduced in the range 322-4000 cm^{-1}. They interpreted this as due to gradually developing gapping in the Fermi surface and consequent removal of carriers. A sum rule was used to argue that N/m^* is about 1/7.5 of its free electron value in the ICDW phase of this material. Benda (1974) had observed spectra at 4.2 K similar to the spectra taken by the above workers at 80 K.

Barker's (1975) infrared reflectivity data can be compared with the high frequency limits of the oscillator fits used to fit the far-infrared data of Fig. 2.6. The fit with $\varepsilon_\infty = 40$ goes to R=0.53, while the fit with $\varepsilon_\infty = 48$ goes to R=0.56 ($R = |(1-\sqrt{\varepsilon_\infty})/(1+\sqrt{\varepsilon_\infty})|^2$). Barkers data are not flat in this frequency range with R=0.52 from 500-1000 cm^{-1}, rising to about 0.57 near 3000 cm^{-1}, falling to 0.50 at 10,000 cm^{-1}, then falling rapidly at higher frequencies. Neither of the present oscillator fits exhibits this behavior. A spread of low energy electronic transitions may be the cause of this non-Drude-like behavior.

B. 1T-$TaSe_2$.

Before discussing the present experiments, it is useful to

compare the present resistivity measurements (Fig. 2.2) with those of others (Wilson et al. 1975, Fig. 1.2). One finds agreement at low temperatures. However at room temperature the present crystals have a higher DC conductivity. This suggests the presence of additional carriers, presumably from an excess of Ta. Our crystals were not directly analyzed for stoichiometry, but they do seem to have an excess of carriers over the best crystals.

Lucovsky et al. (1976) have measured the room temperature reflectivity of 1T-$TaSe_2$ in the infrared. Their reflectivity was lower than the crystals used here. The phonon modes they observed were stronger than those observed here. Both facts can be explained by an excess of carriers increasing the optical conductivity and screening the phonons in the present experiment. They found $\varepsilon_\infty \sim 47$ which was used in some of the fits reported here. The spectra appeared to be a mix of Drude like free carriers and low lying electronic transitions. They did not publish the Drude parameters used in their oscillator fit. Evidence of electronic transitions were not found in the present experiment where the upper frequency limit was 600 cm^{-1}.

Two Drude terms were found to be necessary to fit the background spectrum at 4.2 K in 1T-$TaSe_2$ for frequencies only out to 500 cm^{-1}. In studying 1T-$TiSe_2$, Lucovsky et

al. (1976a) found that two Drude terms were required to fit the spectra of one sample, but only one was required to fit more nearly stoichiometric samples. Hence our slightly underdamped low frequency plasmon ($\bar{\nu}_p$=3000 cm^{-1}, G=700 cm^{-1}) could be associated with off-stoichiometry instead of a Fermi surface with, for instance, two different relaxation times on different sections.

The two Drude fit of Fig. 3.6 has a reflectivity minimum near 750 cm^{-1}, above the limits of the present experiment. The reflectivity of the underdamped plasmon ($\bar{\nu}_p$=2535 cm^{-1}, G=9.3 cm^{-1}), plotted by itself, has a very pronounced minimum near $\bar{\nu}_p/\sqrt{\epsilon_\infty}$ =440 cm^{-1}. Whether a perfectly stoichiometric sample of 1T-$TaSe_2$ would exhibit this behavior is open to question. A relaxation time of $6X10^{-13}$ sec can be calculated from G=9.3 cm^{-1}. This is about thirty times larger than ordinary Cu at room temperature and about 3000 times smaller than very pure Cu at 4.2 K (Kittel 1966).

The temperature dependence of the DC conductivity was measured by Wilson et al. (1975). The order of magnitude decrease in conductivity upon cooling from the ICDW to the CCDW state at 473 K was associated by them with folding the Fermi surface into a Brillouin zone about one thirteenth the size with associated gapping and removal of carriers.

The temperature dependence of the DC conductivity below 473 K is unusual, with a broad minimum at about 300 K. (Fig. 1.2). The explanation probably lies in details of the Fermi surface gapping taking place as well as possible localization effects. Fazekas and Tosatti (1979) have proffered a qualitative explanation of the even more complicated 1T-TaS_2 case in terms of Mott localization.

The present optical work offers further confirmation of these ideas. A Drude fit can in principle separate the relaxation time from the ratio N/m^* which can not be done with measurements of the DC conductivity. From the Drude fits to the 1T-$TaSe_2$ reflectivity described in Chapter 3, one can say that the ratio N/m^* decreases with temperature. This suggests that as the temperature is lowered from 295 K, the effective mass increases or the number of carriers decreases. The Drude parameters used to fit the 295 K spectra had only a lower bound, qualifying such a statement. Certainly the Drude parameters used in the low temperature fits suggest far less than N_o carriers calculated from one electron per unit cell or a very large effective mass, one or both of which vary strongly with temperature. Corroboration of these ideas is hindered by the lack of other transport data for 1T-$TaSe_2$. In section 5A, the behavior of the Hall coefficient of 1T-TaS_2 was seen to imply a strong reduction in the effective number of carriers at lower temperatures.

A reasonable interpretation of the 1T-$TaSe_2$ case might be such as follows. If in the high temperature ICDW phase, there is one electron from each Ta, then $\bar{\nu}_p$=36920 cm^{-1}. Then if gapping destroys 9/10 of the Fermi surface just below 450 K, $\bar{\nu}_p$=12000 cm^{-1}. This is in the range that will fit experiment (Fig. 3.3). The lower values of $\bar{\nu}_p$ observed at the lower temperatures (two carriers, both with $\bar{\nu}_p \sim 3000$ cm^{-1}) then imply that N/m^* is further decreased by a factor of 1/8 as the temperature is lowered to 4.2 K.

This temperature dependence of the fitting parameter $\bar{\nu}_p$ has been observed in a related compound, 1T-$TiSe_2$. In this compound, a transition from an undistorted to a CCDW phase takes place at 200 K. Liang et al. (1979) have measured the temperature dependence of the infrared reflectivity of 1T-$TiSe_2$. They fit their data with enough Lorentz oscillators to fit the prominent phonons together with a single Drude term. They found $\bar{\nu}_p$=8600 cm^{-1} at 300 K actually increase to $\sim$15000 cm^{-1} just above the 200 K transition, then decrease steadily to a stable value of $\sim$1700 cm^{-1} below 130 K. As the Hall coefficient decreases in magnitude by a factor of ten at low temperatures, a single carrier model would imply an effective mass increase by a factor of 2.4.

Liang et al. (1979) also determined ε_∞ as a function of

temperature, finding that it peaked at the 200 K transition temperature. They attributed this to a decrease in the gap energy from CDW formation. ε_∞ was not determined here with sufficient accuracy to draw any conclusions about such an effect in 1T-$TaSe_2$.

Wilson et al. (1978b) have also studied the infrared reflectivity of 1T-$TiSe_2$, concentrating on the free carrier plasmon behavior. To this end, they fit $Im(-1/\varepsilon)$ instead of the reflectivity with an oscillator analysis. Their results were similar to those of Liang et al. (1979). As with Barker's (1975b) earlier work on 1T-TaS_2 and 2H-$TaSe_2$, it was difficult to extract information about the gapping induced by the CDW. An absorption edge at about 1400 cm^{-1} at low temperatures seemed to agree with allowed electronic transitions deduced from band structure calculations of Zunger and Freeman (1978) folded in under the CDW superlattice formation. They experienced difficulty in correlating this with CDW gapping and expressed a desire for relativistic and superlattice band structure calculations.

The prominent dips in the reflectivity at each phonon frequency of 1T-$TaSe_2$ at 4.2 K were seen in Chapter 3 to be associated with an underdamped Drude term. More commonly a rise in the reflectivity is observed near a phonon resonance. Other systems exhibiting such behavior have recently been studied.

Liang et al. (1979) as well as Wilson et al. (1978) have seen large reflectivity dips at each phonon frequency in 1T-$TiSe_2$. This has the mode multiplicty associated with a CCDW-induced superlattice. The dips can be associated with $\bar{\nu} \gtrsim G$. Similar dips in the reflectivity at the phonon frequency of intercalated graphite have been observed by Underhill et al. (1979).

In the present experiments, the behavior of the dips enabled the determination of the plasmon parameters in the oscillator fit to a greater precision than would have been the case had the Lorentz oscillators not been present. In fact, the unusual behavior was not understood until the experiments on 1T-$TaSe_2$ at low temperature were extended out to the high frequency limits of the apparatus. The rapid falloff in reflectivity could not be explained by the Hagen-Rubens relation (3.6). The discovery of the lower than expected value of $\bar{\nu}_p$ for 1T-$TaSe_2$ at temperatures below 100 K is a direct consequence of both the dips at each Lorentz oscillator and the behavior of the background reflectivity. The value of the damping parameter G for 1T-$TaSe_2$ below 100 K made a difference in the size of the dips even though the general background could be explained by a range of values of $\bar{\nu}_p$, G, and ε_∞.

Chapter 6. Summary.

A. Significant findings.

1. CDW-induced mode multiplicity.

The present work describes one of the first observations of CDW-induced phonon mode multiplicity. Ten strong infrared-active phonon modes have been observed in both 1T-TaS_2 and 1T-$TaSe_2$ in their CCDW phases. The 1T-TaS_2 spectrum is remarkably complex, with as many as 31 observed phonon modes. The increased screening by free carriers in 1T-$TaSe_2$ make it possible to see only ten modes. The six highest frequency modes in 1T-$TaSe_2$ have been seen by Lucovsky et al. (1976). Raman spectroscopists have also observed mode multiplicity in these two compounds (Holy 1977, Duffey 1978).

The origin of these modes is believed to be due to the creation by the CDW distortion of a larger unit cell, a 39 atom superlattice, in both these compounds. The atoms in this cell would have 3n-3=114 optic modes. The determination of Raman and infrared selection rules using group theory is a difficult, presently intractable problem. Even the space group of the superlattice has not been reported. The problem is put into perspective by considering the effort required to diagonalize a 117X117 matrix to find the normal modes and coordinates, then

fitting all the force constants to the observed frequencies.

The simpler problem of the undistorted CdI_2-type lattice with a 9X9 matrix has been considered in a simple central force Born-von Karman model by Duffey (1978). From this, the frequencies of modes at points in the Brillouin zone folded back to the zone center under the CDW-induced superlattice formation can be calculated as discussed in Chapter 4. The lack of quantitative agreement between model and experiment points out the necessity for more sophisticated model calculations.

Duffey's (1978) calculation does illustrate the general principles involved and suggests which modes arise from the folding-in of acoustic branches of the phonon dispersion curves. The ratios of frequencies of corresponding modes in 1T-TaS_2 and 1T-$TaSe_2$ agree with this interpretation.

2. Temperature dependence of plasmons.

The temperature dependence of the plasmon fitting parameters for 1T-TaS_2 at 360 K and 295 K revealed nothing that could not have been deduced from the DC conductivity and a carrier density of one per unit cell. This is consistent with reported Hall effect measurements. At 100 K, the 1T-TaS_2 spectra could be explained by a carrier density of about 10^{19} cm^{-3}, in agreement with the reduction noted in Hall effect

measurements. However, a much higher density of carriers was not precluded by the present optical work.

As for 1T-TaS_2, the 1T-$TaSe_2$ spectra taken at higher temperatures could be fit with Drude parameters deduced from the DC conductivity and assuming one carrier per unit cell. However at lower temperatures, the reflectivity of 1T-$TaSe_2$ began to drop off too quickly with frequency for this simple interpretation. An underdamped two plasmon fit with a relatively long relaxation time was needed to fit the data. In this case, the real and imaginary parts of the Drude contribution to the dielectric constant are of comparable magnitude. This in turn causes a dip to appear in the reflectivity at each resonance of each Lorentz oscillator used to fit the phonons instead of the more commonly observed peak.

The reduction of the plasma frequency fitting parameter $\bar{\nu}_p$ with decreasing temperature was interpreted in Chapter 5 as due either to a decrease in the effective number of carriers or decrease in the averaged effective mass. Both are probably due to CDW-induced alterations to the band structure as the temperature is lowered. The difficulty of a band structure calculation in the CCDW phase is comparable to the calculation of the phonon dispersion curve.

B. Suggestions for future research.

In all but the CCDW phase of both 1T-TaS_2 and 1T-$TaSe_2$, no phonons were observed in either the reflectivity or dual-cavity spectra. It is possible to mechanically alternate either the beam or sample so that for half a cycle the detector measures the sample, while for the other half it measures the reference. The lock-in amplifier will then directly measure the difference between sample and reference reflectivity. When the sample is almost as reflecting as the reference, this has the advantage of directly measuring the quantity of interest, namely small deviations from Drude-like reflectivity. However the dual-cavity technique used here also brings out weak structure. It would be interesting to compare the two methods; one with many reflections, the other with only two experimentally subtracted from one another.

Another experiment worth doing is measuring the reflectivity of 1T-$TaSe_2$ versus temperature at higher frequencies. This would show whether the minimum in the reflectivity at 750 cm^{-1} predicted by the low frequency oscillator fits actually exists. Crystals of differing stoichiometries could also be studied to determine if the second plasmon is due to additional carriers caused by excess Ta.

Appendix I.

Linear-chain model for the CdI_2 structure E_u mode.

The normal modes for the CdI_2 structure are shown in Fig. 1.3. If the two I atoms are denoted by 1 and 3 and the Cd ion by 2, the equations of motion for the E_u mode may be written as follows.

$$-m_1 \omega^2 u_1 - C(u_2 - u_1) = -eE \qquad (I.1)$$

$$-m_1 \omega^2 u_3 - C(u_2 - u_3) = -eE \qquad (I.2)$$

$$-m_2 \omega^2 u_2 - C(u_1 + u_3 - 2u_2) = 2eE \qquad (I.3)$$

E is the macroscopic field and e is the macroscopic effective charge -e on the anions and +2e on the cations. C is the force constant between Cd and I. The I-I force constant does not contribute because adjacent atoms oscillate in phase in the E_u mode. The u_i are the displacements from equilibrium.

These three coupled equations may be combined to give equations identical to those of a diatomic linear chain by making the following substitutions.

$$2x_1 = (u_1 + u_3);\ M = 2m_1;\ m = m_2$$

$e_T^*=2e;\ x_2=u_2;\ u=x_1-x_2$

Adding (I.1) and (I.2) along with the above sustitutions gives

$$-m\omega^2 x_2-2C(x_1-x_2)=e_T^* E$$

$$-M\omega^2 x_1-2C(x_2-x_1)=-e_T^* E. \qquad (I.4)$$

These are identical to the macroscopic equations for a linear chain diatomic lattice (Kittel 1966). The two equations can be subtracted to give

$$-\bar{m}\omega^2 u-2Cu=e_T^* E \qquad (I.5)$$

where u was defined above and m is the reduced mode mass,

$$\bar{m}=mM/(m+M)=2m_1m_2/(2m_1+m_2). \qquad (I.6)$$

e_T^* is the macroscopic effective charge on the cation (Cd), half of this being on each anion.

The ionic polarization is given by $P_i=ne_T^*u$ where n is the number of ion pairs per unit volume. If the total polarization can be written as the sum of ionic and electronic

terms,

$$P=P_i+n\alpha_o E=(\varepsilon-1)/4\pi \qquad (I.7)$$

then

$$\varepsilon(\omega)=\varepsilon_\infty+4\pi n e_T^{*2}/\bar{m}/(\omega_o^2-\omega^2)= \varepsilon_\infty+S\omega_o^2/(\omega_o^2-\omega^2) \qquad (I.8)$$

where $S=\varepsilon(0)-\varepsilon_\infty$, $\omega_o^2=2C/\bar{m}$, and $\varepsilon_\infty=1+4\pi n\alpha_o$. (I.8) is of the Lorentz form when damping is neglected. e_T^* for this model may be calculated from experimentally determined parameters as

$$e_T^*/e=\left[c\,\bar{\nu}_o/e\right](\pi\bar{m}S/n)^{1/2} \qquad (I.9)$$

where $\bar{\nu}_o$ is in cm^{-1}.

Bibliography.

Agnihotri, O. P., Seghal, H. K., and Garg, A. K. 1973. Solid State Commun. 12, 135.

Ashcroft, N. W. and Mermin, N. D. 1976. Solid State Physics (Holt, Rinehart and Winston, New York).

Barker, A. S. Jr. 1966. Optical Properties and Electronic Structure of Metals and Alloys. edited by F. Abeles. (North Holland, Amsterdam).

Barker, A. S. 1975. Private communication.

Barker, A. S. Jr., Ditzenberger, J. A. and DiSalvo, F. J. 1975a. Phys. Rev. B 12, 2049.

Bayard, M. and Sienko, M. J. 1976. Journal of Solid State Chem. 19,325.

Benda, J. A. 1974. Phys. Rev. B 10, 1409.

Bevington, P. R. 1969. Data Reduction and Error Analysis for the Physical Sciences (McGraw-Hill, New York).

Bromley, R. A. 1971. Phil. Mag. 23, 1417.

Burstein, E. 1967. Dynamical Processes in Solid State Optics. edited by R. Kubo and H. Kamimura (W. A. Benjamin, New York).

Burstein, E., Pinczuk, A. and Wallis, R. F. 1971. The Physics of Semimetals and Narrow-gap Semiconductors. edited by D. L. Carter and R. T. Baye (Pergamon Press, Oxford).

Chang, I. F., Mitra, S. S., Plendl, J. N., and Mansur, L. C. 1968. Phys. Status Solidi 28, 663.

Chantry, G. W. 1971. Submillimetre Spectroscopy (Academic Press, New York).

Craven, R. A. and Meyer, S. F. 1977. Phys. Rev. B 16, 4853.

DiSalvo, F. J., Maines, R. G., Waszczak, J. V. and Schwall, R. E. 1974. Solid State Commun. 14, 497.

DiSalvo, F. J., Wilson, J. A., Bagley, B. G. and Waszczak, J. V. 1975. Phys Rev. B 12, 2220.

DiSalvo, F. J., Moncton, D. E. and Waszczak, J. V. 1976. Phys. Rev. B 14, 4231.

DiSalvo, F. J. and Graebner, J. E. 1977. Solid State Commun. 23,

825.

DiSalvo, F. J. and Rice, T. M. 1979. Physics Today, 32, April.

Dorner, B., Ghosh, R. E. and Harbeke, G. 1976. Phys. Stat. Sol. 73, 655.

Donovan, B., and Angress, J. F. 1971. Lattice Vibrations (Chapman and Hall, London).

Duffey, J. R., Kirby, R. D. and Coleman, R. V. 1976, Solid State Commun. 20, 617.

Duffey, James R. 1978. Thesis. (University of Nebraska, unpublished).

Fately, Wm. G., Dollish, F. R., McDevitt, N. T., and Beatty, F. F. 1972. Infrared and Raman Selection Rules for Molecular and Lattice Vibrations: The Correlation Method (John Wiley and Sons, New York).

Fazekas, P. and Tosatti, E. 1979. Phil. Mag. B 39, 229.

Friend, R. H., Jerome, D., Liang, W. Y., Mikkelsen, J. C. and Yoffe, A. D. 1977. J. Phys. C, 10, L705.

Hodgson, J. N. 1970. Optical Absorption and Dispersion in Solids (Chapman and Hall, London).

Holy, J. A. 1977. Thesis (University of Illinois, unpublished).

Holy, John A., Klein, M. V., McMillan, W. L. and Meyer, S. F. 1976. Phys. Rev. Lett. 37, 1145.

Holy, J. A., Woo, K. C., Klein, M. V. and Brown, F. C. 1977. Phys. Rev. B 16, 3268.

Inada, R., Onuki, Y. and Tanuma, S. 1979. Phys. Lett. 69A, 453.

Jaswal, S. S. 1979. Phys. Rev. B15, 20, 5297.

Karecki, D. R. 1975. Unpublished.

Karecki, D. R. and Clayman, B. P. 1976, Solid State Commun. 19, 479.

Karecki, D. R. and Clayman, B. P. 1979, Phys. Rev. B15, 19, 6367.

Kittel, Charles. 1966. Introduction to Solid State Physics, second edition (John Wiley and Sons, New York).

Klein, M. V., Holy, J. A. and Meyer, S. F. 1976. Bull. Am. Phys. Soc. 21, 338.

Lamb, W. E. Sr. 1946. Phys. Rev. 70, 308.

Liang, W. Y., Lucovsky, G. and Mikkelsen, J. C. 1979. Phil. Mag. B39, 133.

Lockwood, P. J. 1969, Light Scattering in Solids, edited by G. B. Bright (Springer, New York).

Lucovsky, G., White, R. M., Benda, J. A. and Revelli, J. F. 1973 . Phys. Rev, B 7, 3859.

Lucovsky, G., Liang, W. Y., White, R. M. and Pisharody, K. R. 1976. Solid State Commun. 19, 303.

Lucovsky, G., White, R. M., Liang, W. Y. and Mikkelsen, T. L. 1976a. Phil. Mag. 34, 907.

Mead, D. G. and Irwin, J. C. 1977. Can. J. Phys. 55, 379.

Moncton, D. E., Axe, J. D. and DiSalvo, F. J. 1975. Phys. Rev. Lett. 34, 734.

Moncton, D. E., DiSalvo, F. J., Axe, J. D., Sham, L. J. and Patton, R. 1976. Phys. Rev. B15. 14, 3432.

Moncton, D. E., Axe, J. D. and DiSalvo, F. J. 1977. Phys. Rev. B. 16, 801.

Nathan, M. I., Shafer, M. W. and Smith, J. E. Jr. 1972. Bull. Am. Phys. Soc. 17, 336.

Rice, M. J. and Strassler, S. 1974. Solid State Commun. 13, 1931.

Richards, P. L. and Tinkham, M. 1960. Phys. Rev. 119, 575.

Sai-Halasz, G. A. and Perry, P. B. 1977. Solid State Commun. 21,995.

Scruby, C. B., Williams, P. M. and Parry, G. S. 1975. Phil. Mag. 31, 255.

Sears, W. M., Klein, M. L. and Morrison, J. A. 1979. Phys. Rev. B15, 19, 2305.

Smith, J. E. Jr., Nathan, M. I., Shafer, M. W. and Torrance, J. B. 1972. The Eleventh International Conference on the Physics of Semiconductors, Warsaw (unpublished).

Smith, J. E.; Tsang, J. C. and Shafer, M. W. 1976. Solid State Commun. 19, 283.

Steigmeier, E. F., Harbeke, G. and Audeset, H. 1976. Solid State Commun. 20, 667.

Stirling, W. G., Dorner, B. Cheeke, J. D. W. and Revelli, J. 1976. Solid State Commun. 18, 931.

Tanuma, S., Suematsu, H., Higuchi, K., Inao, R. and Onuki, Y. 1978. The Application of High Magnetic Fields in Semiconductor Physics. edited by J. F. Ryan (Oxford University Press).

Tanuma, S., Inada, R. and Onuki, Y. 1979. Physics and Chemistry of Layered Materials. The Science Reports of the Research Institutes, Tohuku University. Series A, Volume 27 Supplement No. 1. Edited by Yuichiro Nishima.

Tatlock, G. J. 1977. Developments in Electron Microscopy and Analysis. edited by D. L. Misell (Institute of Physics, Bristol).

Templeton, T. L. 1973. Thesis (unpublished, Simon Fraser Univ.).

Thompson, A. H., Gamble, F. R. and Revelli, J. F. 1971. Solid State Commun. 9, 981.

Thompson, A. H., Pisharody, K. R. and Koehler, R. F. 1972. Phys. Rev. Lett. 29, 163.

Tidman, J. P., Singh, O., Curzon, A. E. and Frindt, R. F. 1974. Phil. Mag. 30, 1191.

Tidman, J. P. and Frindt, R. F. 1976. Can. J. Phys. 54, 2306.

Tsang, J. C., Smith, J. E. Jr. and Shafer, M. W. 1976. Phys. Rev. Lett. 37, 1407.

Tsang, J. C., Smith, J. E., Shafer, M. W. and Meyer, S. F. 1977. Phys. Rev. B. 16, 4239.

Tsang, J. C., Smith, J. E. Jr and Shafer, M. W. 1978. Solid State Commun. 27, 145.

Uchida, S., Tanabe, K., Okajima, K. and Tanaka, S. 1979. Physics and Chemistry of Layered Materials. The Science Reports of the Research Institutes, Tohuku University. Series A, Volume 27, Supplement No. 1. Edited by Yuichiro Nishima.

Underhill, C., Leung, J. Y., Dresselhaus, G. and Dresselhaus, M. S. 1979. Solid State Commun. 29, 769.

Van der Walk, H. J. L. and Haas, C. 1977. Phys. Stat. Sol. (b). 80, 321.

Verble, J. L. and Wieting, T. J. 1972. Solid State Commun. 11, 941.

Van der Pauw, L. J. 1958. Philips Tech. Rev. 20, 220.

Wakabayashi, N., Smith, H. G. and Nicklow, R. M. 1975. Phys. Rev. B. 12, 659.

Wang, C. S. and Chen, J. M. 1974. Solid State Commun. 14, 1145.

Ward, R. W. 1976. Infrared Physics. 16, 385.

Wieting, T. J. and Verble, J. L. 1971. Phys. Rev. B. 3, 4286.

Wieting, T. J. 1973. Solid State Commun. 12, 931.

Wieting, T.J. and Verble, J.L. 1979. Electrons and Phonons in Layered Crystal Structures. Edited by T.J. Wieting and Michael Schluter (D. Reidel. Dordrecht: Holland).

Williams, P. M. 1976. Crystallography and Crystal Chemistry of Materials with Layered Structures. edited by F. Levy (Reidel, Dordrect-Holland).

Wilson, J. A. and Yoffe, A. D. 1969. Adv. in Phys. 18, 193.

Wilson, J. A., DiSalvo, F. J. and Mahajan, S. 1975. Adv. in Phys. 24, 117.

Wilson, J. A. 1978. Phys. Stat. Sol. (b). 86, 11.

Wilson, J. A. 1978a. Phys. Rev. B15. 17,3880.

Wilson, J. A., Barker, A. S. Jr., DiSalvo, F. J. Jr. and Ditzenberger, J. A. 1978b. Phys. Rev. B15, 18, 2866.

Wyckoff, R. W. G. 1963. Crystal Structures (Interscience, New York).

Ziebeck, K. R. A., Dorner, B., Stirling, W. G. and Schollhorn, R. 1977. J. Phys. F: Metal Phys. 7, 1139.

Ziman, J. M. 1969. Principles of the Theory of Solids (Cambridge University Press, London).

Zunger, A. and Freeman, A. J. 1978. Phys. Rev. B15, 17, 1839.